




Article

# An Alternative Scenario on the Origin of Ultra-High Pressure (UHP) and Super-Reduced (SuR) Minerals in Ophiolitic Chromitites: A Case Study from the Mercedita Deposit (Eastern Cuba)

Núria Pujol-Solà <sup>1,\*</sup>, Joaquín A. Proenza <sup>1</sup> , Antonio Garcia-Casco <sup>2,3</sup>,  
José María González-Jiménez <sup>2</sup> , Aleu Andreazini <sup>4</sup>, Joan Carles Melgarejo <sup>1</sup>  and  
Fernando Gervilla <sup>2,3</sup>

<sup>1</sup> Departament de Mineralogia, Petrologia i Geologia Aplicada, Facultat de Ciències de la Terra, Universitat de Barcelona, Martí i Franquès s/n, 08028 Barcelona, Spain; japrozena@ub.edu (J.A.P.); joan.carles.melgarejo.draper@ub.edu (J.C.M.)

<sup>2</sup> Departamento de Mineralogía y Petrología, Facultad de Ciencias de la Tierra, Universidad de Granada, Avda. Fuentenueva, s/n, 18071 Granada, Spain; agcasco@ugr.es (A.G.-C.); jmgonzj@ugr.es (J.M.G.-J.); gervilla@ugr.es (F.G.)

<sup>3</sup> Instituto Andaluz de Ciencias de la Tierra (CSIC-UGR), Avda. de las Palmeras 4, 18100 Armilla, Granada, Spain

<sup>4</sup> Centro de Instrumentación Científica, Universidad de Granada, Campus Universitario de Fuentenueva, Paseo Prof. Juan Ossorio, s/n, 18003 Granada, Spain; aleuan@gmail.com

\* Correspondence: npujolsola@ub.edu; Tel.: +34-93-402-1341

Received: 31 July 2018; Accepted: 27 September 2018; Published: 1 October 2018



**Abstract:** The origin of the assemblage of ultra-high pressure (UHP), super-reduced (SuR) and several crustally derived phases in ophiolitic chromitites is still hotly debated. In this paper, we report, for the first time, this assemblage of phases in ophiolitic chromitites of the Caribbean. We studied the Mercedita chromitite deposit in the eastern Cuban ophiolitic complexes. The mineral phases were characterized using microRaman spectroscopy, energy-dispersive spectroscopy with a scanning electron microscope (SEM-EDS), X-ray microdiffraction and electron microprobe analyses. Mineral concentrates were prepared using hydroseparation techniques. We have identified oriented clinopyroxene lamellae in chromite, oriented rutile lamellae in chromite, moissanite hosted in the altered matrix of the chromitite, graphite-like amorphous carbon, corundum and SiO<sub>2</sub> hosted in healed fractures in chromite grains, and native Cu and Fe–Mn alloy recovered in heavy-mineral concentrates obtained by hydroseparation. This assemblage may correspond to UHP–SuR conditions, implying recycling of chromitite in the mantle or formation of the chromite grains at deep mantle depths, followed by emplacement at a shallow level in the mantle. However, the chromitite bodies contain gabbro sills oriented parallel to the elongation of the chromitite lenses, and these show no evidence of HP/UHP metamorphism. Therefore, the identified “exotic” phases may not be indicative of UHP. They formed independently as oriented clinopyroxene lamellae in chromite during cooling (clinopyroxene and rutile), in super-reduced microenvironments during the serpentinization processes, and by transference of subducted crustal material to the mantle wedge via cold plumes.

**Keywords:** moissanite; inclusions; Mercedita; serpentinization; super-reducing conditions; chromitites; ophiolites; Cuba

## 1. Introduction

Minerals indicative of super-reducing (SuR) environments, e.g., native elements, alloys, carbides, nitrides and phosphides, and those formed at ultra-high pressure (UHP), e.g., diamond, TiO<sub>2</sub>-II, pseudomorphs after coesite and stishovite, are increasingly being reported in peridotites and associated chromitites from ophiolite complexes, along with minerals that typically form in the continental crust, e.g., zircon, quartz, K-feldspar, almandine, andalusite, apatite and kyanite [1–12]. The origin of minerals considered “exotic” to the ophiolitic rocks is currently the subject of many frontline studies and remains a hotly debated topic.

Some investigators have proposed that peridotites and associated chromitites form near the MTZ-Moho Transition Zone (petrologic Moho) in a suprasubduction environment and incorporate crustal minerals in the shallow mantle. The rocks are subsequently recycled into the ultra-deep mantle (>410 km, and perhaps even deeper, to a mantle-core depth) by continued subduction, where SuR and UHP minerals become incorporated, e.g., [6,13–15]. Rapid exhumation of the deep-seated chromitites and host peridotites carrying SuR, UHP and continental-crust-derived minerals is related to the generation of low-viscosity upwelling channels created during the opening of marginal basins in island arcs or continental arcs as a result of retraction of subducting slabs during the rollback process [14,15]. In this model, crustal minerals are already present in the chromitite, which forms in a mantle wedge contaminated by subducted material with a crustal component after the ascent of cold plumes derived from the subducting slabs [12,16].

Others have suggested that SuR, UHP and continental-crust-derived minerals correspond to material present in the slab graveyard located at the bottom of the upper mantle, near the mantle-transition zone. This subducted material is incorporated in chromite crystallizing from melts originating from rising deep-seated mantle plumes [5,6,17,18] or, alternatively, asthenosphere-derived melts that rise along slab-windows [4,19].

In addition, the role of fluids has been highlighted [20] in the formation of ophiolitic chromite deposits. According to this metasomatic model, localized super-reducing environments favor the disequilibrium crystallization of UHP minerals, forming very unusual paragenesis in the oceanic crust. The authors propose that chromite formation requires a SuR subsolidus in a low-pressure environment with a temperature above 800 °C.

Yet other investigators [21,22] have synthesized SuR and UHP mineral assemblages from plasma generated by electric discharges at >5700 °C, suggesting that these minerals in ophiolitic rocks can originate after obduction by lightning strikes. This short review indicates that the SuR and UHP assemblages may not record a deep origin and may not support an emplacement history involving mantle lithologies.

Here, we provide the first-ever report of SuR minerals in ophiolitic rocks from the Caribbean, in fact from the Mercedita chromitite deposit, in eastern Cuba. This mineral assemblage, which occurs with continental-crust-derived minerals, is described and evaluated in the framework of chromitite genesis during the formation and geological evolution of the Caribbean region. Our work leads to an evaluation of the various models proposed for the origin of this unusual paragenesis.

## 2. Geological Setting

The Mercedita chromitite deposit is located in eastern Cuba (Figure 1a), part of the Mayarí-Baracoa ophiolitic belt. It is associated with Cretaceous HP serpentinite-matrix subduction mélanges (Sierra del Convento and La Corea), Early to Late Cretaceous volcanic arc sequences, and a Late Cretaceous metamorphic sole (the Güira de Jauco Amphibolite Complex) related to the onset of ophiolite obduction [16,23–39] (Figure 1a,b). The synorogenic La Picota and Mícara formations date oceanic arc-terrane collision and exhumation during latest Cretaceous to earliest Paleocene times, prior to the final northeasterly verging collision with the Bahamas platform and accretion of tectonic pile onto the North American plate (Figure 1b) [23,27,28,35,36]. The Cuban Ophiolite Belt represents oceanic lithosphere obducted onto the North American continental paleomargin owing to northward collision

between the Caribbean plate and the passive margins of the Maya block and the Bahamas platform during the latest Cretaceous to Late Eocene [23,27,28].

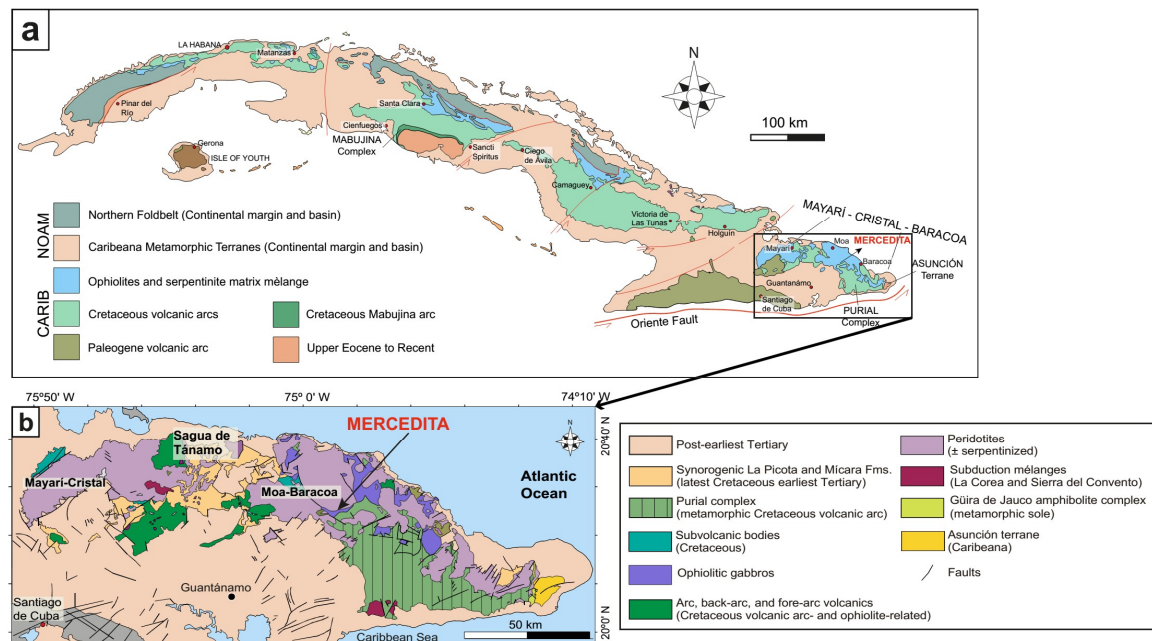


**Figure 1.** (a) Generalized geologic-tectonic map of Cuba; (b) Schematic geological map of the Mayarí-Baracoa Ophiolitic Belt (MBOB) showing the location of the Mercedita Mine.

### 2.1. Eastern Cuba Ophiolites

The Mayarí-Baracoa ophiolite belt, in the eastern part of the Cuban Ophiolite Belt, outcrops for more than 1000 km along the Cuban coastline (Figure 1a,b) and represents the largest exposure of oceanic lithosphere in the circum-Caribbean region, e.g., [24,37]. The allochthonous Mayarí-Baracoa belt is divided by major fault zones into two different massifs: the Mayarí-Cristal massif in the west and the Moa-Baracoa massif in the east (Figure 1b), having mantle sections of more than 5 km and about 2.2 km in thickness respectively [24,38]. The ophiolite assemblage is highly dismembered; the dominant lithology is harzburgitic tectonite with subordinate dunite, chromitite, layered gabbro and discordant microgabbro, pyroxenite, troctolite, wehrlite, and diabase bodies [24,37–39] in both massifs. The Cuban ophiolites have supra-subduction zone geochemical signature [24,38,40–42] related to the intra-oceanic Greater Antilles arc, developed during the lower to upper Cretaceous.

### 2.2. The Moa-Baracoa Ophiolitic Massif

The Moa-Baracoa ophiolitic massif consists of harzburgitic tectonites with minor dunite and the petrologic Moho crosscut by gabbroic dikes associated with layered gabbros. These lithologies are in tectonic contact with pillow basalts of the Morel Formation (88–91 Ma), which have a back-arc geochemical affinity and are related to cumulate gabbros [25,40,42]. These findings strongly indicate a back-arc environment scenario for the formation of the Moa-Baracoa massif [30,33,40,41].

Numerous high-Al ( $0.41 < Cr\# < 0.54$ ) chromitite bodies are hosted in the mantle tectonites [24]. These bodies have tabular to lenticular shape, are concordant to the host peridotite foliation, and show a dunite envelope of variable thickness [24]. The melts inferred to have been in equilibrium with such Al-rich chromitite are similar in composition to back-arc basin basalts (BABB) [24,41,43].

### 2.3. The Mercedita Deposit

The Mercedita deposit, located in the most southerly part of the Moa-Baracoa massif (Figure 1b), is considered the largest and most important podiform chromite deposit in America [44], with

calculated reserves exceeding 5 million tons. The largest chromitite body is 600 m long, 250 m wide, and up to 20 m thick [24,44]. Tabular to lenticular bodies of chromitite of variable size (Figure 2a) are crosscut by normal faults. The lenses are invariably parallel to the foliation and lineation of host peridotite and are located in the mantle-crust transition zone, characterized by the interlayering of ultramafic and gabbroic rocks. Dunite (from few centimeters to a few meters in thickness) systematically envelopes the chromitite bodies, though chromitite-harzburgite contacts are locally developed. The contact between chromitite and peridotites is generally sharp and only locally gradational [44].

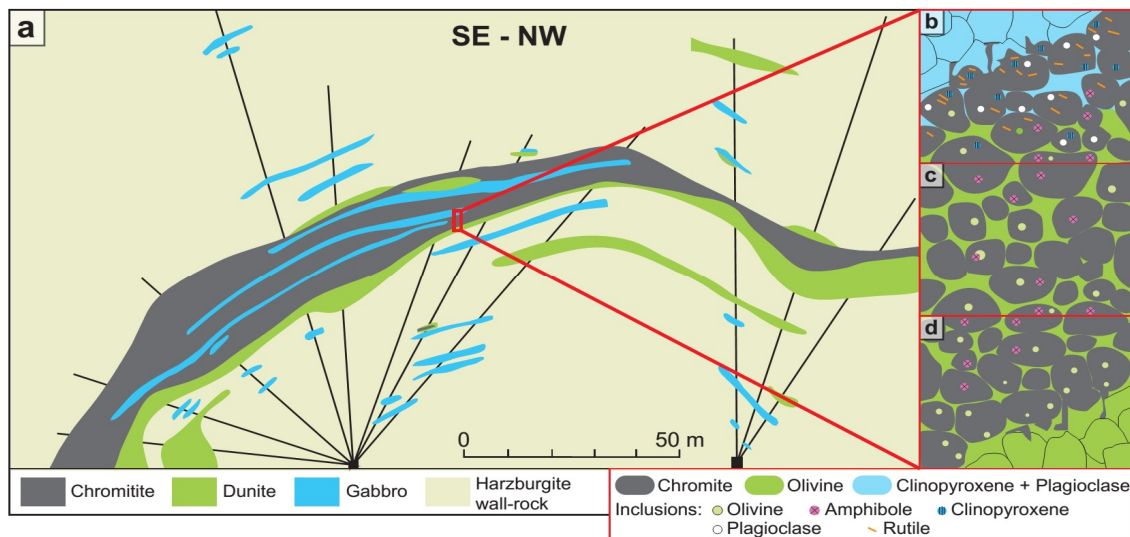


**Figure 2.** (a) Cross-section through the Mercedita chromitite. The relationships between chromitite, dunite, gabbros and harzburgite were interpreted from holes drilled upward from the roof of the mine's galleries; (b) Mineral inclusions in Mercedita chromite grains near the contact with gabbro; (c) Mineral inclusions in Mercedita chromite grains in the inner part of the chromitite body; (d) Mineral inclusions in Mercedita chromite grains near the dunite envelope. (b–d) Are not to scale.

The chromitite lenses usually include gabbro sills of variable size (Figure 2a), from centimeters to >100 m in length. These have the same orientation as the chromitite bodies [44]. The layers of gabbro are locally replaced by the chromitite, an observation also supported by the chemical variations observed in the composition of chromite, which shows increasing Ti and Al towards the gabbro bodies [24]. Later gabbro and pegmatitic gabbro dikes crosscut the chromitite bodies and are sheared or displaced by normal faults with NE-SW and NW-SE orientations [24,44]. Interestingly, similar relationships between chromitites and gabbro sills parallel to the chromitite bodies have been described in nearby Cayo Guam chromite deposit (Moa-Baracoa massif, Cuba [45]), Camagüey (Cuba [46]), and in the Coto Block (Philippines [47]).

Chromitite shows two types of texture [44]: massive compact and massive anhedral chromite in an altered olivine matrix. However, other textures include deformed nodular, mylonitic (locally in shear zones) and cataclastic (locally along normal faults) varieties. Pull-apart fractures are abundant in the lenses.

### 3. Materials and Methods

#### 3.1. Sampling

50 thin sections from chromite samples (including drill cores) collected from the Mercedita high-Al chromitite deposit have been selected and carefully studied for this article.

### 3.2. Hydroseparation

Chromitite samples (2.7 kg) were crushed and powdered using an agate mill. The powder was sieved using various mesh-sizes and hydroseparated (HS Lab, Barcelona, Spain). The grains obtained were mounted as polished monolayers (five concentrates) on resin blocks (SimpliMet 1000). For details of the procedure, see [48].

### 3.3. Scanning Electron Microscopy (SEM)

After studying the polished thin sections with petrographic microscope, selected samples were examined with a scanning electron microscope (SEM) using both a Quanta 200 FEI XTE 325/D8395 and a JEOL JSM-7100 field-emission scanning electron microscope equipped with an energy-dispersive spectrometer (EDS) at the Serveis Científics i Tecnològics, Universitat de Barcelona (CCiTUB), Spain. The operating conditions were 15 keV accelerating voltage and 5 nA in backscattered electron (BSE) mode.

### 3.4. MicroRAMAN Spectroscopy

The “exotic” mineral phases were characterized using microRaman directly in the polished thin sections with a HORIBA Jobin LabRaman HR 800 dispersive spectrometer equipped with an Olympus BXFM optical microscope in the Serveis Científics i Tecnològics, Universitat de Barcelona (CCiTUB). Raman spectra were obtained using a non-polarized 532 nm laser, a 100× objective, with five measurements lasting 10 s. The Si band at  $\sim 520\text{ cm}^{-1}$  was used for calibration. The spectra were processed using the LabSpec<sup>®</sup> software (Jobin Yvon) (Villeneuve-d’Ascq, France).

### 3.5. Electron Microprobe Analysis (EMP)

Electron microprobe analyses of chromite were carried out using a CAMECA SX-50 electron microprobe at the Serveis Científics i Tecnològics, Universitat de Barcelona (CCiTUB). The instrument is equipped with four wavelength-dispersive spectrometers (WDS) and one energy-dispersive spectrometer (EDS). The WDS analyses were performed using an acceleration voltage of 20 keV, a beam current of 15 nA, a beam diameter of 1–2  $\mu\text{m}$  and a dwell time of 10 s. Calibration standards were  $\text{Cr}_2\text{O}_3$  (Cr), corundum (Al), rutile (Ti), periclase (Mg), hematite (Fe), rhodonite (Mn), NiO (Ni), and metallic V. The detection limits were 350 ppm for Cr, 100 ppm for Al, 250 ppm for Ti, 180 ppm for Mg, and 150 ppm for Fe, Mn, Ni and V. The PAP correction procedure [49] was used for obtaining concentrations.

### 3.6. X-ray Micro Diffraction

Moissanite crystals were analyzed on the thin section by X-ray microdiffraction ( $\mu\text{XRD}$ ) using a D8 DISCOVER  $\mu\text{MR}$  powder diffractometer in Bragg–Brentano  $\theta/2\theta$  geometry of 154.1 mm of radius, Cu  $K\alpha_1$  radiation ( $\lambda = 1.54056\text{ \AA}$ ), operated at 50 kV and 1 mA, and with a 0.1 mm collimator at the Centro de Instrumentación Científica (CIC) of the University of Granada. During analysis, the sample was spun at 1 revolution per minute. Crystals were scanned from  $25^\circ$  to  $56^\circ 2\theta$  with a step size of  $0.02^\circ$  and a time of 240 s per step, using a Pilatus3-100K Detector (Villigen, Switzerland) at a distance of 151.58 mm. The software Diffrac.EVA was used to integrate the frames and generate the diffractograms, to detect the peaks, and to assign mineral phases and their corresponding  $d_{\text{hkl}}$  to each peak.

## 4. Results

### 4.1. Ore Texture and Mineralogy

The chromitite lenses (Figure 2) mainly consist of subhedral to anhedral grains of chromite 0.5 mm to 1 cm across, and intergranular olivine partially or completely altered to serpentine-group minerals and minor chlorite (Figure 2c,d). The serpentine phase displays a pseudomorphic mesh

texture after olivine, indicating that lizardite is the main phase. However, in some samples chrysotile and antigorite were also recognized [50]. The chromite grains contain inclusions of euhedral olivine (50–200  $\mu\text{m}$ ) and amphibole (30–100  $\mu\text{m}$ ) (Figure 2c). Other accessory mineral phases are Fe–Ni sulfides (commonly, millerite) and platinum-group minerals (PGM: laurite, irarsite). The inclusions in chromite are generally monomineralic and randomly distributed in the grains, even though they can appear locally clustered or aligned. Olivine inclusions are more abundant near the contact with the dunite envelope (Figure 2d) and show the same optical orientation as olivine crystals in dunite, indicating dunite replacement by chromitite, previously documented by [44].

Near the contact with gabbro sills a <10 cm transition zone develops where chromite “invades” the intergranular space between clinopyroxene and plagioclase grains of the gabbro (Figure 2b). In this zone, clinopyroxene and plagioclase inclusions (<100  $\mu\text{m}$ ) in chromite crystals are common; the clinopyroxene inclusions are in optical continuity with clinopyroxene crystals of the adjacent gabbro, indicating that chromitite replaced the gabbro sills [44].

Chromitites are affected by two stages of post-magmatic evolution: serpentinization and chloritization. Serpentinization produced the partial to total replacement of olivine by serpentine-group minerals, magnetite and Fe–Ni sulfides. A second stage produced a thin rim of ferrian chromite, chlorite and sulfides of Ni (millerite) and Cu (chalcopyrite, chalcocite).

Far from the alteration-induced rim and cracks, the spinel consists of high-Al chromite [ $0.42 < \text{Cr}\# = \text{Cr}/(\text{Cr} + \text{Al}) < 0.53$ ;  $0.58 < \text{Mg}\# = \text{Mg}/(\text{Mg} + \text{Fe}^{2+}) < 0.77$ ] (Table 1). Its composition is generally homogeneous (except for lens 6), overlapping the compositional field of podiform “ophiolitic” chromitite (Figure 3a,d). The ranges of concentration of major element oxides are (in wt %): 34.76–42.5  $\text{Cr}_2\text{O}_3$ , 24.44–33.14  $\text{Al}_2\text{O}_3$ , 12.96–18.51  $\text{MgO}$ , up to 6.36  $\text{FeO}$ , 8.21–16.92  $\text{Fe}_2\text{O}_3$ , 0.07–0.28  $\text{V}_2\text{O}_3$ , 0.02–0.29  $\text{NiO}$ , and up to 0.34  $\text{MnO}$ . The  $\text{TiO}_2$  contents are variably high (0.12–0.48 wt %, Figure 3b), overlapping that of chromite crystallized from MORB-type basalts (Figure 3c). This is explained by the fact that the BABB melts from which chromite crystallized had analogous compositions to MORB-type melts [55].

**Table 1.** Representative electron microprobe analyses of chromite from the Mercedita mine.

Sample	G-12-27	G-12-6	G-12-2	G-12-8	G-12-12	G-12-18	G-15-4	L2-7	L2-8	L3-2	L3-8	L3-7	L3-11	L6-1
<b>TiO<sub>2</sub></b> (wt %)	0.33	0.33	0.33	0.33	0.40	0.28	0.31	0.31	0.32	0.20	0.21	0.29	0.20	0.28
<b>Al<sub>2</sub>O<sub>3</sub></b>	31.03	31.02	31.77	30.53	31.38	30.49	30.44	29.37	29.56	32.04	32.78	31.19	32.98	26.19
<b>V<sub>2</sub>O<sub>3</sub></b>	0.16	0.16	0.15	0.19	0.18	0.14	0.10	0.19	0.15	0.14	0.09	0.16	0.07	0.19
<b>Cr<sub>2</sub>O<sub>3</sub></b>	37.02	36.49	35.88	37.25	38.30	35.80	37.42	36.88	37.09	35.11	35.29	36.20	35.77	41.22
<b>Fe<sub>2</sub>O<sub>3</sub> *</b>	3.38	3.43	3.19	3.14	0.00	3.14	3.35	4.61	3.56	4.18	3.74	2.88	2.01	4.18
<b>FeO *</b>	11.73	11.62	11.12	11.98	14.47	16.92	11.09	12.29	12.55	11.37	9.88	11.85	11.35	11.17
<b>MgO</b>	16.59	16.50	16.90	16.29	14.10	12.96	16.82	15.84	15.55	16.82	17.84	16.21	16.75	16.26
<b>MnO</b>	0.17	0.21	0.12	0.11	0.18	0.30	0.13	0.25	0.26	0.08	0.16	0.16	0.20	0.17
<b>NiO</b>	0.17	0.13	0.18	0.20	0.24	0.10	0.14	0.13	0.14	0.20	0.20	0.18	0.24	0.23
<b>Sum</b>	100.59	99.90	99.64	100.02	99.25	100.13	99.81	99.89	99.21	100.14	100.18	99.12	99.57	99.89
<b>Ti (a.p.f.u.)</b>	0.06	0.06	0.06	0.06	0.07	0.05	0.05	0.06	0.06	0.04	0.04	0.05	0.03	0.05
<b>Al</b>	8.48	8.52	8.70	8.41	8.75	8.56	8.37	8.16	8.26	8.74	8.85	8.63	9.00	7.35
<b>V</b>	0.03	0.03	0.03	0.03	0.03	0.03	0.02	0.04	0.03	0.03	0.02	0.03	0.01	0.04
<b>Cr</b>	6.78	6.72	6.59	6.88	7.17	6.74	6.90	6.87	6.95	6.42	6.40	6.72	6.55	7.76
<b>Fe<sup>3+</sup></b>	0.59	0.60	0.56	0.55	0.00	0.56	0.59	0.82	0.64	0.73	0.64	0.51	0.35	0.75
<b>Fe<sup>2+</sup></b>	5.73	5.73	5.85	5.67	4.97	4.60	5.85	5.56	5.49	5.80	6.10	5.67	5.78	5.77
<b>Mg</b>	0.03	0.04	0.02	0.02	0.04	0.06	0.03	0.05	0.05	0.01	0.03	0.03	0.04	0.03
<b>Mn</b>	2.27	2.27	2.16	2.34	2.86	3.37	2.16	2.42	2.49	2.20	1.89	2.33	2.20	2.22
<b>Ni</b>	0.03	0.02	0.03	0.04	0.04	0.02	0.03	0.02	0.03	0.04	0.04	0.03	0.04	0.04
<b>#Cr</b>	0.44	0.44	0.43	0.45	0.45	0.44	0.45	0.46	0.46	0.42	0.42	0.44	0.42	0.51
<b>#Mg</b>	0.72	0.72	0.73	0.71	0.63	0.58	0.73	0.70	0.69	0.73	0.76	0.71	0.72	0.72

a.p.f.u. = atoms per formula unit; \*: Calculated.

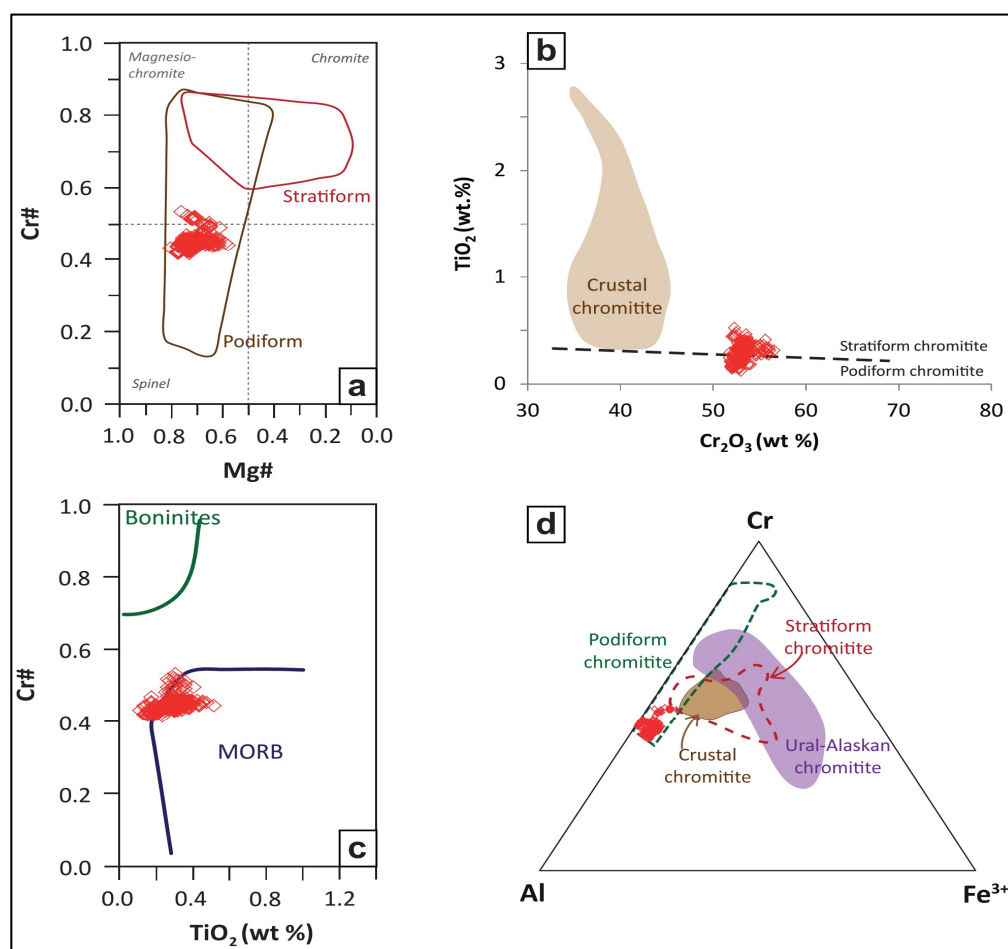


**Figure 3.** Mercedita chromite composition diagrams: (a) Cr# [Cr/(Cr + Al)] versus Mg# [Mg/(Mg + Al)]; (b) TiO<sub>2</sub> versus Cr<sub>2</sub>O<sub>3</sub> (wt %) diagram showing the compositional fields for podiform, stratiform and crustal chromitite; (c) Cr# versus TiO<sub>2</sub> (wt %) showing the type of melt in equilibrium; (d) Fe<sup>3+</sup>-Cr-Al ternary diagram showing the fields for different types of chromitites. Compositional fields are after [51,52] in (a), after [53,54] in (b), (d) and after [55] in (c).

#### 4.2. Mineral Inclusions Identified In Situ in the Chromitite

##### 4.2.1. Oriented Clinopyroxene and Rutile Lamellae in Chromite

Submicrometric lamellae of clinopyroxene with a preferred crystallographic orientation are included in chromite grains located far from the interaction zone with the gabbro dikes (Figure 4a–c). These elongate crystals are usually 10 μm long and less than 1 μm wide, follow the (111) crystallographic planes of chromite (Figure 4b,c) and are variably distributed in most of the samples studied. The energy-dispersive spectra obtained using the field-emission electron microscope (FESEM) on relatively large grains (e.g., Figure 4d) indicate a diopside or Ca-rich enstatite composition (the signal of the host chromite is recorded in the spectra to some extent), but further Raman analyses show spectra compatible with diopside (Figure 4e, after subtracting the chromite signal), with peaks at 242, 326, 391, 667, 857, 1011 and 1269 cm<sup>-1</sup>, which are analogous with those described by [12,56].

Rutile lamellar crystals 5–80 μm across are present in chromite following the (111) crystallographic plane (Figure 5a,b,d). The elongate crystals define three different main orientations in chromite (Figure 5b). The EDS spectra obtained in the larger crystals (Figure 5c) clearly show that only Ti and O are present; the Raman spectra show peaks at 239, 246, 441 and 609 cm<sup>-1</sup> (Figure 5e) corresponding to rutile (e.g., RUFF ID: R110109). However, it is noteworthy that rutile inclusions are only found in chromite grains located near the contact with the gabbro sills described by [24,44].

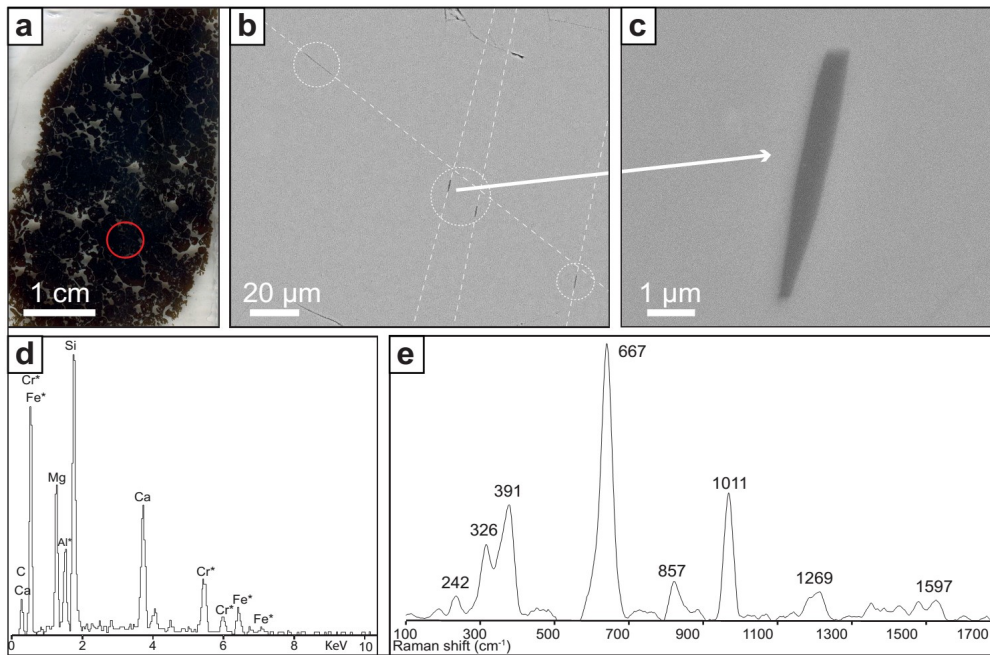


**Figure 4.** Oriented clinopyroxene lamellae in the Mercedita chromite: (a) Thin section containing the clinopyroxene lamellae showed in the images (b,c). The location of the studied lamellae is showed with a red circle; (b) Backscattered electron (BSE) image of oriented pyroxene lamellae defining two main directions; (c) Zoom of one sub-micron clinopyroxene lamellae of image (b); (d) Energy-Dispersive Spectroscopy (EDS) spectra of the clinopyroxene of image (b), showing qualitatively its chemical composition. The elements marked with an asterisk correspond to the chromite host; (e) Raman spectra of the diopside after subtraction of the chromite background.

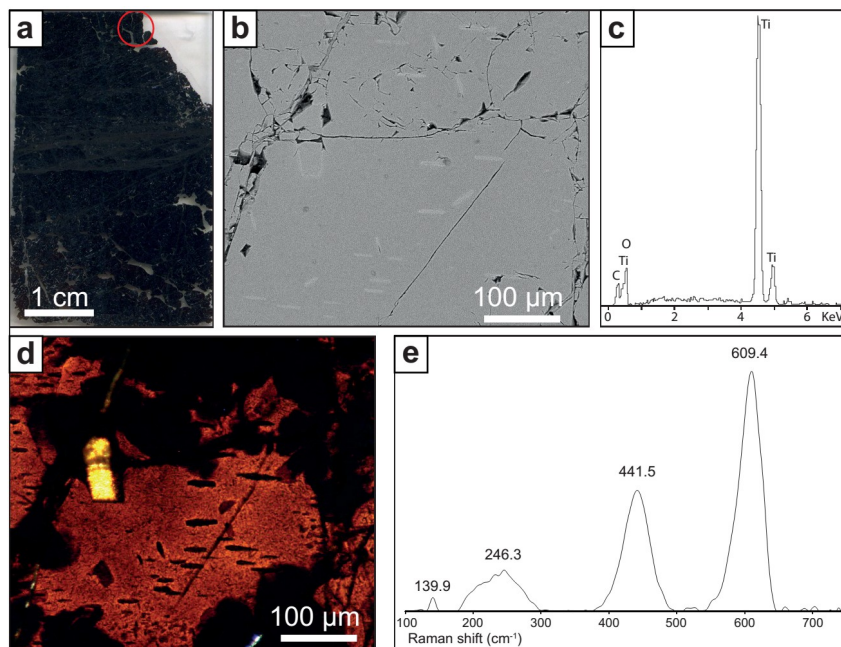


**Figure 5.** Rutile laminar crystals oriented in the Mercedita chromite in contact with the gabbro: (a) Thin section containing the rutile crystals in the images (b,d). The location of the images (b,c) is shown with a red circle; (b) Backscattered electron (BSE) image of oriented rutile crystals defining three main directions; (c) Energy-Dispersive Spectroscopy (EDS) spectra of the rutile of image (b), showing qualitatively its chemical composition; (d) Transmitted light optical microscope image of rutile crystals included in chromite; (e) Raman spectra of rutile after subtraction of the chromite background.



#### 4.2.2. Mineral Inclusions in Healed Fractures in Chromite

Chromite grains host multiple trails of inclusions (Figure 6a–c) that can be followed across several grains. The inclusions range from a submicrometric size to 7  $\mu\text{m}$ . The mineral species hosted in these trails are described hereafter.

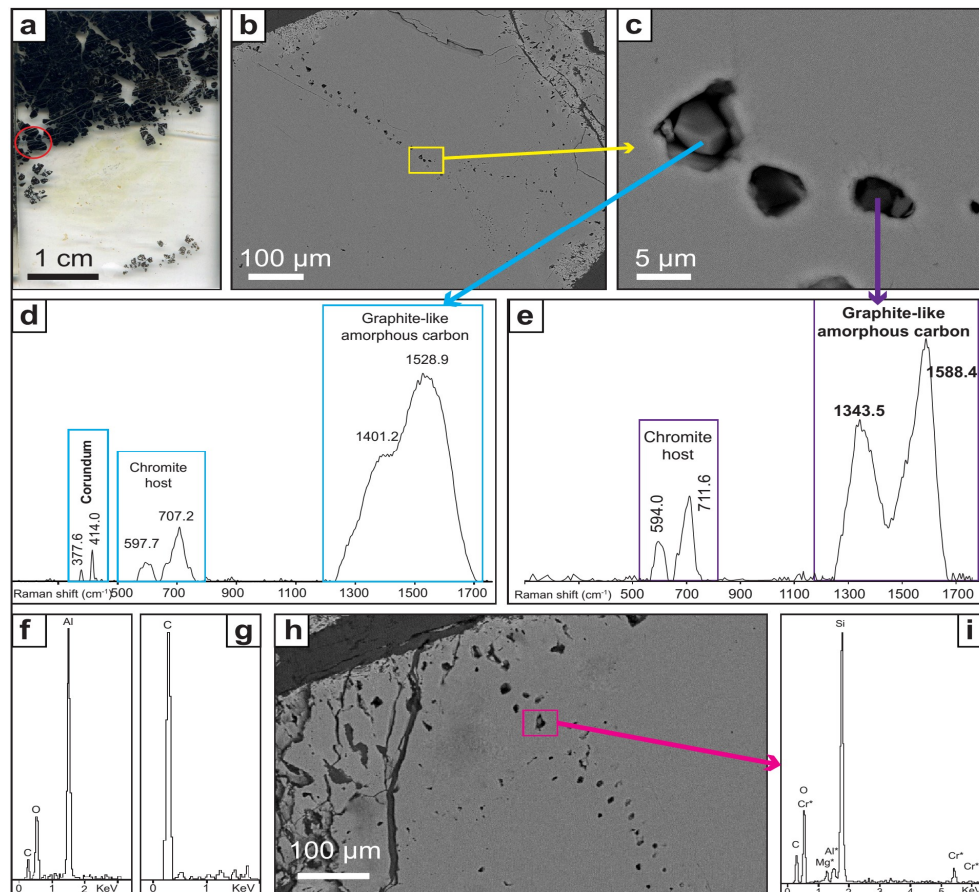


**Figure 6.** Inclusion trails in chromite grains: (a) Thin section containing the inclusion trails in images (b,c). The location of the inclusions in the section is shown with a red circle; (b) Backscattered electron (BSE) image of a trail of inclusions; (c) Detail of three inclusions hosting corundum and graphite-like amorphous carbon, BSE image. (d) Raman spectra of corundum, the host chromite and graphite-like amorphous carbon surrounding the corundum crystal; (e) Raman spectra of the carbon-bearing inclusion in image (c), showing the host chromite and graphite-like amorphous carbon; (f) Energy-Dispersive Spectroscopy (EDS) spectra of the corundum crystal of image (d), showing qualitatively its chemical composition; (g) Energy-Dispersive Spectroscopy (EDS) spectra of the carbon-bearing inclusion in image (c); (h) BSE image of inclusion trail close to the chromite alteration rim; (i) Energy-Dispersive Spectroscopy (EDS) spectra of the  $\text{SiO}_2$  crystal of image (h), showing qualitatively its chemical composition.

Subhedral corundum grains up to 5  $\mu\text{m}$  in size (Figure 6c) have been characterized by Raman spectroscopy (Figure 6d, in which the characteristic spectrum appears together with that of the host chromite), and by EDS (Figure 6f). Corundum is surrounded by amorphous carbon, which also appears in the Raman spectra.

Carbon inclusions up to 5  $\mu\text{m}$  across are common in the chromite trails (Figure 6c). The main species of carbon is graphite-like disordered carbon, which is characterized by the D and G Raman bands at about 1350 and 1580  $\text{cm}^{-1}$ , respectively (Figure 6d,e). The inclusions show a variable degree of disorder in the stacking sequence. The EDS spectra of these inclusions show that C is the only element present (Figure 6g).

Grains of  $\text{SiO}_2$  also have been identified (Figure 6h,i). These inclusions, up to 7  $\mu\text{m}$  across, are usually located close to the ferrian chromite rims. They have been characterized by EDS (Figure 6i). However, it has not been possible to obtain the corresponding Raman spectra owing to strong fluorescence.

#### 4.2.3. Moissanite in the Silicate Matrix

Moissanite crystals have been found in situ in two replicated thin sections (elaborated after the same rock slab) (Figure 7a). The SiC grains are located in the altered matrix of chromitite (Figure 7b,c) that mainly consists of aggregates of fine-grained hydrated minerals including serpentine-group minerals, clinocllore and minor hornblende.

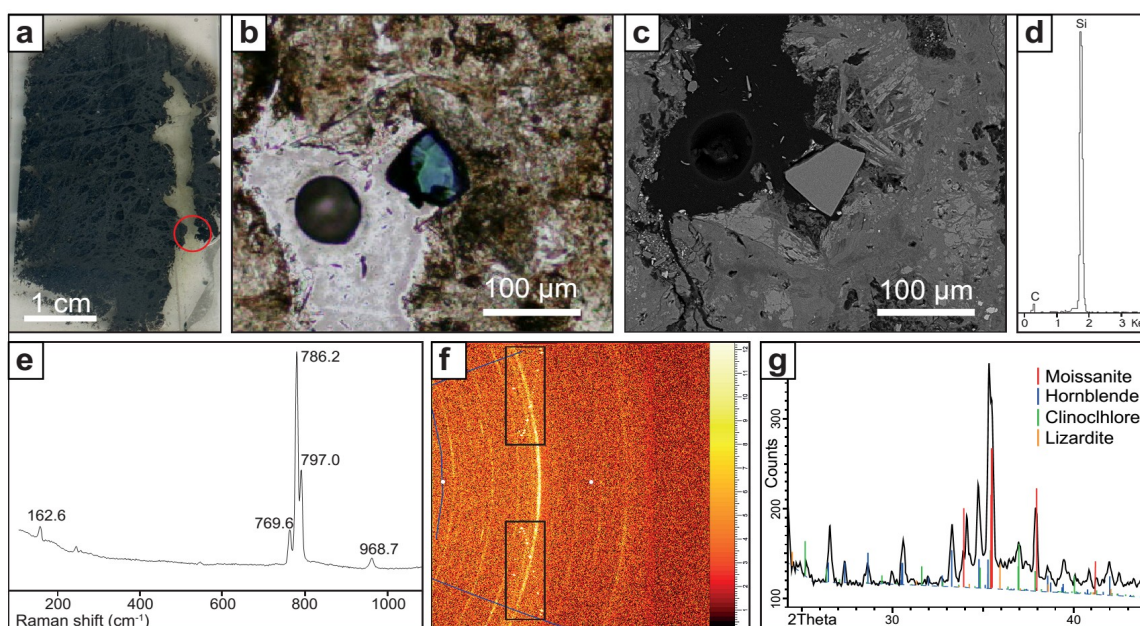


**Figure 7.** Moissanite crystal hosted in the chromitite altered silicate matrix: (a) Thin section containing the moissanite crystal in images (b,c). The location of the moissanite crystal in the thin section is showed with a red circle; (b) Transmitted light optical microscope image of the moissanite crystal. Note that the crystals show the typical natural moissanite blue color; (c) Backscattered electron (BSE) image of the same moissanite crystal in (b); (d) Energy-Dispersive Spectroscopy (EDS) spectra of the moissanite crystal of images (b,c), showing qualitatively its chemical composition; (e) Raman spectra of the moissanite crystal; (f) Single crystal X-ray microdiffraction pattern of moissanite; (g) Integration of the diffraction pattern with peak identification.

The crystals are subhedral, with a grain size of about 80  $\mu\text{m}$  (Figure 7b,c) showing the typical blue color in transmitted light. The EDS spectra show peaks of Si and C only (Figure 7d). The Raman spectra, with peaks at 162, 769, 786, 797 and 968  $\text{cm}^{-1}$ , confirms that the mineral is moissanite. Single crystal X-ray microdiffraction (Figure 7f) shows that SiC has a hexagonal structure that corresponds to the  $6H$  polytype (Figure 7g), the most common polytype of moissanite [57].

Synthetic SiC used in polishing the sample has a maximum grain-size (21.8  $\mu\text{m}$ —P800) significantly smaller than that of the observed moissanite crystals (up to 80  $\mu\text{m}$ ). We believe that the sample was not contaminated during thin-section preparation. In addition, moissanite grains with similar morphological characteristics (crystal, habit size and color) have been reported from the chromitites of various Neotethyan ophiolites (e.g., Oman, Ponzati-Karsanti in Turkey, Luobusa, Sarohay and Hegenshan in Tibet and Ray-Iz in Polar Urals [4,19,58–60]). These grains have been interpreted as natural moissanite and not due to anthropogenic contamination.

### 4.3. Mineralogy of Heavy Mineral Concentrates Obtained by Hydroseparation

Euhedral grains of native Cu up to 100  $\mu\text{m}$  (Figure 8a,b) are very common in the mineral concentrates. Even though the EDS spectra of these grains show a small oxygen peak (Figure 8b), electron-microprobe analyses show that the grain is native Cu (99–100 wt % Cu). Unidentified inclusions up to 15  $\mu\text{m}$  in length and rich in P and Na are hosted in the native Cu grains (Figure 8c). To our knowledge, their qualitative composition does not correspond to any known mineral. The grains also show an overgrowth of  $\text{SiO}_2$  (Figure 8d).

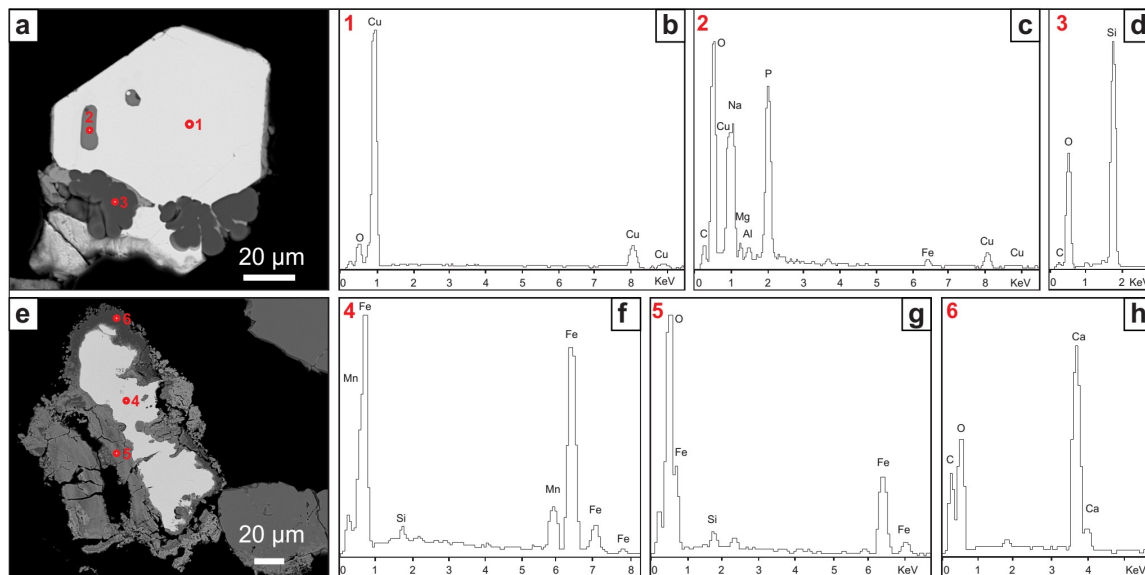


**Figure 8.** Metallic alloys found in the mineral concentrates of chromitite samples: (a) Backscattered electron (BSE) image of a metallic grain showing inclusions and mineral growth in the lower border. Numbers indicate the position of the EDS spectra of images (b–d); (b) Energy-Dispersive Spectroscopy (EDS) spectra of center of the bright grain of image (a) (1); (c) EDS spectra of the inclusion (2); (d) EDS spectra of the mineral growth in the lower border of the crystal (3); (e) Backscattered electron (BSE) image of a metallic grain surrounded by other mineral phases. Numbers indicate the position of the EDS spectra of images (f–h); (f) EDS spectra of center of the bright grain of image (e) (4); (g) EDS spectra of the border (5); (h) EDS spectra of the outer border of the crystal (6).

Elongate grains (up to 125  $\mu\text{m}$ ) of a Fe–Mn alloy (Figure 8e) have been characterized by EDS (Figure 8f; the Si peak corresponds to the glue used to mount the grains in the polished section). These grains are surrounded by an inner layer of Fe oxide (Figure 8g) and an outer layer of Ca-carbonate (Figure 8h). The texture indicates a replacement relationship.

In addition, it should be mentioned that euhedral grains of zircon have been identified [16] in heavy-mineral concentrates from the Mercedita chromitites.

## 5. Discussion

### 5.1. Origin of Oriented Clinopyroxene and Rutile Lamellae in Chromite

The Mercedita chromitites contain inclusions of clinopyroxene with preferred orientation in chromite, a petrographic feature that has been observed in other ophiolitic chromitites (Table 2). Such inclusions have been interpreted as the exsolution of silicate components lodged in the structure of high-temperature and high-pressure chromite (or their high-pressure polymorphs) [6,61,62], whether these pyroxene lamellae are associated [61] or not [12,63] with minerals that typically form at high pressure (e.g., coesite >30 GPa; [64] and references therein). According to the models proposed in the literature, such petrographic feature could correspond to (1) chromite that originated at low

pressure in the shallow mantle, and then experienced recycling in the deep mantle, at which point they could dissolve a silicate component. Once returned to the surface, the new spinel reverted back to low-pressure chromite and released the dissolved silicate component in the form of pyroxene lamellae [12,14,15,61,63,65]. It is also possible (2) that a high-pressure polymorph of chromite already containing high amounts of SiO<sub>2</sub> and CaO in its structure had crystallized near the bottom of the upper mantle or at the mantle transition and was carried upwards by deep-seated mantle plumes or asthenospheric melts, that experienced decompression to low-pressure chromite while releasing clinopyroxene lamellae, e.g., [6,19].

These interpretations seem to be consistent with the results of recent experimental work; magnesiochromite can incorporate only <0.5 wt % CaO at 12–15 GPa and minor amounts (<1–2 wt %) of SiO<sub>2</sub> at <16 GPa, whereas the structure of the high-pressure polymorph calcium ferrite (CF-type, CaFe<sub>2</sub>O<sub>4</sub>) can accommodate higher amounts of SiO<sub>2</sub> (~3–5 wt % at 14–18 GPa in the MgCr<sub>2</sub>O<sub>4</sub>–Mg<sub>2</sub>SiO<sub>4</sub> system and up to ~11–14 wt % in the MgAl<sub>2</sub>O<sub>4</sub>–Mg<sub>2</sub>SiO<sub>4</sub> system) and CaO (~7–8 wt % at 14–18 GPa) [66,67]. The calcium ferrite polymorph is stable in the P-T region between 12.5 and 20 GPa at ~1400–1600 °C, and it could release SiO<sub>2</sub> and CaO in the form of pyroxene lamellae upon decompression [66–68].

It is worth noting that we have not identified exsolution-induced lamellae of coesite or other UHP minerals in the Mercedita chromitite (Table 2). This lack of coesite in our samples can be related to the mechanism of formation of the clinopyroxene lamellae. Silica will only exsolve from chromite once CaO and SiO<sub>2</sub> have been completely consumed to form clinopyroxene and MgSiO<sub>3</sub> [66]. Therefore, the absence of coesite lamellae in the Mercedita chromitites may simply reflect the fact that not all the CaO and SiO<sub>2</sub> were consumed.

However, the Mercedita chromitites are juxtaposed to, and also include, gabbro sills that show no evidence of HP/UHP metamorphism, ruling out the recycling of the whole ophiolitic sequence, including chromitite, gabbro and their dunite envelope and host harzburgite. In turn, the Mercedita chromitite could consist of an accumulation of UHP chromite grains brought from the lower mantle to the top of the petrologic Moho upon its arrival to the shallow part of the lithosphere, as suggested by [6,19]. We must point out that there is no evidence for such magmatic activity related to mantle plume in eastern Cuba ophiolites [40,42], leading us to rule out this possibility. In addition, the Mercedita chromite grains yielded micro-Raman spectra with positions at 591–596 and 712–717 cm<sup>-1</sup>, which are similar to the peaks observed for low-pressure cubic chromite and magnesiochromite and strongly differ from the peaks observed in the high-pressure chromite polymorph (Figure 9), which suggests that they were not derived from a high-pressure polymorph. In any case, clinopyroxene exsolution in chromite grains do not necessarily involve exsolution from a UHP phase. In fact, the liquidus chromite can concentrate significant amount of SiO<sub>2</sub> and CaO (~0.3 wt % each) that is more than enough to exsolve clinopyroxene lamellae during solid-state processes of annealing (see [22]).

Another interesting observation is that chromite grains in the vicinity of gabbro sills juxtaposed or included in the Mercedita chromitite body also contain rutile lamellae with preferred crystallographic orientation. These types of inclusions have been described in chromitites of the Bushveld layered complex in South Africa [69] as well as in other ophiolitic chromitites, e.g., [70]. Such type of inclusions is interpreted as the result of exsolution of TiO<sub>2</sub> from the chromite structure upon cooling, owing to the low solubility of Ti in the structure of chromite at a low temperature [70,71]. The presence of these inclusions in Mercedita chromite indicates that the contact between the gabbro sills and the chromitites was a reaction zone with a relatively high availability of titanium. Since the composition of chromite is broadly constant except in the proximity of the gabbros (see profiles in Figure 4 in [24], the local increase in Ti must be attributed to the presence of the gabbros.

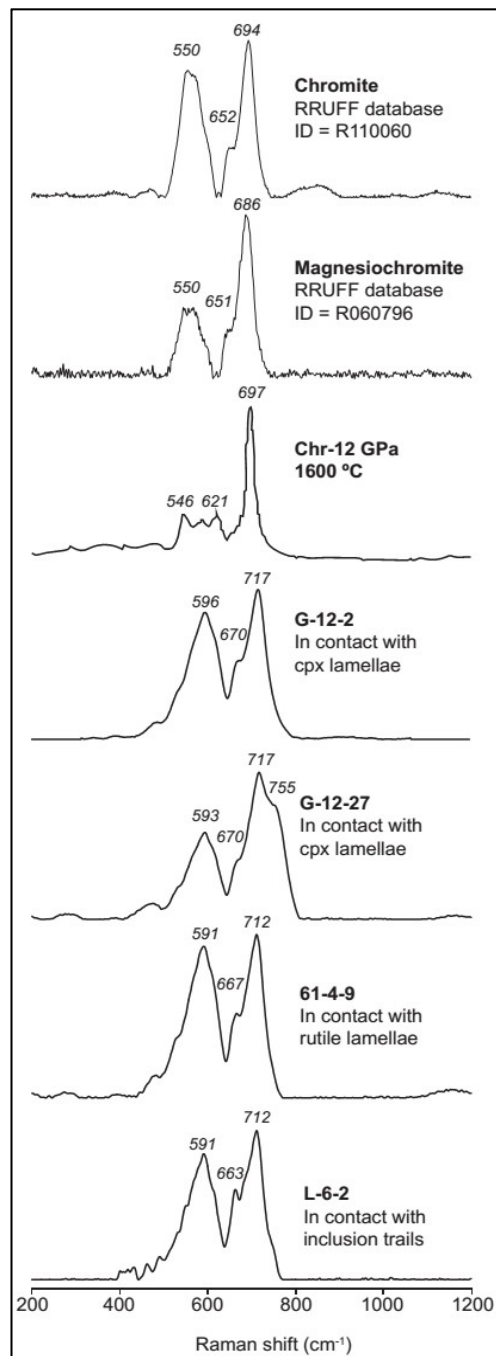


**Figure 9.** Raman spectra of chromite in the Mercedita chromitites. Spectra of chromite and magnesiochromite from natural examples and experimental works are shown by comparison. The spectrum for high-pressure chromite polymorph (Chr-12 GPa, 1600 °C) is from [67].

**Table 2.** Occurrence of UHP (Ultra-High Pressure), SuR (Super-Reduced) and Crustal-derived “exotic” mineral phases in worldwide ophiolites and chromitites. Luobusa (Tibet), Dingqing (Tibet) and Ray-Iz (Polar Urals) data is from [15,72] and references therein, Purang (Tibet) data from [73], Zedang (Tibet) data from [74], Semail (Oman) data from [4,62], Mirdita (Albania) data from [75], Ponzati-Karsanti (Turkey) data from [10], Orhaneli-Harmancik (Turkey) data from [11], Myitkyina (Myanmar) data from [76], Baja California (Mexico) data from [12] and Moa-Baracoa (Cuba) data from [16] and this study.

Ophiolite	Luobusa (Tibet)	Dingqing (Tibet)	Purang (Tibet)	Zedang (Tibet)	Ray-Iz (Polar Urals)	Semail (Oman)	Mirdita (Albania)	Pozanti-Karsanti (Turkey)	Orhaneli-Harmancik (Turkey)	Myitkyina (Myanmar)	Baja California (Mexico)	Moa-Baracoa (Cuba)
Host Rock	Chrom, Harz	Harz	Peridotite	Chrom, Dun	Chrom, Harz	Chrom	Chrom	Chrom	Chrom	Peridotite	Chrom	Chrom, Harz
Diamond	×	×	×		×		×	×		×		
Coesite/Stishovite pseudomorph	×				×							
TiO2 II ( $\alpha$ -PbO <sub>2</sub> structure)	×											
Cubic-BN	×											
Si-rutile	×											
BWJ (inverse-spinel structure)	×											
CF-chromite Clinopyroxene exsolution lamellae	×			×	×	×			×		×	×
Amorphous carbon	×				×							×
Moissanite (SiC)	×	×	×		×	×	×	×		×		×
Fe-carbide (FeC)	×				×							
W-carbide (WC)	×				×							
Ti-carbide (TiC)	×				×							
Fe-silicide (FeSi)	×				×							
Ti-nitride (TiN)	×				×							
TAZ (Ti <sub>4</sub> Al <sub>2</sub> (Zr,Si)O <sub>11</sub> )	×											
Native Si	×				×					×		
Native Ni, Co, Ce, Fe, Cr, Zn, PGE	×		×		×							×
Iron-Wustite (Fe-FeO)	×	×			×		×					
Alloys (Fe-Mn, Fe-Cr, Fe-Co)	×				×							×
Alm garnet	×				×	×						
Andalusite	×				×							
Amphibole	×			×	×	×						
Apatite	×				×	×						
Biotite	×											
Corundum	×	×			×	×	×					×
K-feldspar	×					×						
Kyanite	×				×							
Ilmenite	×				×							
Muscovite	×											
Plagioclase	×				×							
Quartz	×				×	×						×
Rutile	×				×	×		×		×		×
Titanite	×				×	×						
Zircon	×	×			×	×	×	×		×	×	×

×: Indicates the presence of the mineral in the ophiolite (peridotites and/or chromitites).

### 5.2. The SuR Assemblage

The Mercedita chromitite contains moissanite (SiC), native Cu and a Fe–Mn alloy surrounded by an iron oxide and CaCO<sub>3</sub> (Figures 7 and 8). Similar phases have been reported in other ophiolitic chromitites (Table 2) and interpreted as part of a super-reducing (SuR) assemblage [3,4,6–8,10,14,15,17]. Although only recently reported in ophiolitic chromitites [58,77], moissanite has already been found in a variety of terrestrial and extraterrestrial rocks, including meteorites [78] and references therein, kimberlites and associated diamond [57,79–82], volcanic breccias and tuff [72,83,84], high- and low-grade metamorphic rocks [59,85], and limestones [86,87]. According to experimental and empirical data, the formation of SiC only occurs at a fugacity of oxygen 6.5–7 log units below the iron-wüstite buffer (IW) [88,89]. This observation, together with the common association of the SiC with inclusions of native Si and other minerals such as diamond and coesite that typically form at UHP conditions, has led some authors [3,6,15] to suggest that moissanite found in ophiolitic peridotites and chromitites formed from highly reducing fluids present near the top of the Mantle Transition Zone. However, some [89] have shown that moissanite can be deposited at low pressure and low temperature (3.5 GPa and <700–800 °C) by ultra-reducing fluids released during the initial stages of serpentinization of olivine in peridotites. In this model, C-rich fluids provided by dehydration of the sedimentary lid of the subducting slab reacted with peridotite, trapping H<sub>2</sub>O in the hydrous alteration-induced minerals and thus progressively reducing fluids. CH<sub>4</sub>-rich fluids are associated with serpentinization of ultramafic rocks in the submarine and subduction zone environments. CH<sub>4</sub> fluid inclusions occur in olivine from partially serpentinized harzburgite and dunite [90]. Production of CH<sub>4</sub> during serpentinization in the sub-seafloor is a widely accepted process [91]. In addition, CH<sub>4</sub> can be generated as a by-product of serpentinization of peridotites in the mantle wedge overlying the subducting oceanic slab, as a result of the complete consumption of water during formation of serpentine [90] and references therein.

The observation of large crystals of moissanite up to 80 µm across in the serpentinized silicate matrix of Mercedita chromitites is consistent with their formation related to serpentinization fluids. Furthermore, the presence of C in the system during serpentinization is also consistent with inclusions of graphite-like amorphous carbon in sealed cracks in many Mercedita chromite grains. These highly reducing fluids released during serpentinization may be also responsible for the formation of native Cu grains and the Fe–Mn alloy, which are stable at ΔFMQ between –9 and –12, as suggested by [92] for the ophiolitic chromitites of Kempirsai and [89] for the Luobusa chromitites. In addition, Ref. [93] described Fe–Ni and Ni–P alloys that also record extremely low conditions of oxygen fugacity and interpreted them to result from serpentinization.

### 5.3. Minerals Typical of the Continental Crust

Mineral concentrates from the Mercedita chromitite contain zircon, corundum, and quartz (Table 2). According to [16], zircon yields an age between 289 ± 9 Ma (early Permian) and 310 ± 10 Ma (late Carboniferous), much older than the time of ophiolite formation (90–125 Ma); [23,25]. The zircon contains a suite of inclusions (monazite, K-feldspar, quartz, biotite, apatite and occasional ilmenite) typical of any zircon crystallized from a crustal magma. A crustal origin of the zircon is also consistent with its Hf isotopic composition, with εHf(t) ranging from –5.57 to –3.67 [16]. Interestingly, xenocrystic zircon of the same age has been reported in associated oceanic gabbros and volcanic arc lavas in Cuba [94] indicating the recycling of crustal zircon through the mantle wedge above the paleo-subducting slab of the Greater Antilles Arc.

### 5.4. Pros and Cons of Existing Models in Order to Explain the SuR and Associated Minerals in Mercedita

Table 2 summarizes the occurrence of UHP, SuR and crustal-derived phases discovered in chromitites and associated peridotites from the mantle section of ophiolitic complexes. Various models have been proposed to explain the presence of these “exotic” minerals.

(i) The Subduction-Recycling Model.

Chromitites and host peridotites are formed at shallow depth; the assemblage is subducted into the Mantle Transition Zone, and later exhumed to a shallow depth together with its host dunite and harzburgite at spreading centers as a mantle diapir [9,13–15,63]. In this model, SuR phases and coexisting UHP minerals are incorporated into chromitite during the UHP event at the Mantle Transition Zone, whereas the crustal minerals are trapped during crystallization of chromite at low pressure in the upper mantle [12,14,15]. This model has been largely considered to explain the mineral phases found in the Luobusa chromitites (Tibet). However, it has limitations. It does not explain the presence of unmetamorphosed gabbro sills included in the Mercedita chromitites. Moreover, it cannot explain why SuR minerals are closely linked to serpentinization-related minerals, which are not stable at the Mantle Transition Zone or even shallower depths.

(ii) The Plume Model.

Chromite grains formed from high-Cr magmas in the Mantle Transition Zone (15–16 GPa and 1600 °C, [6]) or the lower part of the upper mantle are proposed to encapsulate UHP and SuR phases. Later, these grains migrate upward in a mantle plume and are incorporated in the magma system beneath a spreading center [5,6,17,18,66,95]. According to this model, crustal minerals encapsulated in chromitite were brought to the MTZ through earlier subduction, and SuR and UHP minerals formed at or near the top of the MTZ. This model has been used to explain the mineral phases recovered in the Ray-Iz ophiolitic chromitites (Polar Urals [6]). However, besides requiring an specific geological setting of mantle plume plus spreading center, recent experimental studies [67] have shown that Cr is preferentially partitioned into garnet at pressure conditions of the MTZ, preventing chromite (or its high-pressure polymorph) to directly crystallize from melts at these depths. Moreover, it has been suggested that chromite (or its high-pressure polymorph) is not stable at the reducing conditions of the MTZ, and that such conditions would imply a complete loss of oxygen, forming aluminum spinel and native Cr and Fe [89]. As with the previously discussed model, this model has limitations as well. It fails to explain the formation of the mineral phases in the Mercedita chromitite. Firstly, the model predicts the formation of Cr-rich chromite, whereas the Mercedita chromite is Al-rich. Secondly, the model cannot explain the presence of gabbros juxtaposed and included in the chromitite. Thirdly, there is no evidence of magmatic activity related to mantle plume in eastern Cuba ophiolites. Finally, it does not explain the coexistence of serpentinization-related minerals with SuR phases.

(iii) The Slab Contamination Model.

The presence of continental crust-derived minerals in chromitites and ophiolites reflects the subduction of metasedimentary rocks. These rocks were subducted into the deep mantle and reacted with highly reduced phases. Later, rollback and breakoff of a subducting slab creates a slab window through which asthenosphere rises and melts, generating Cr-rich mafic magmas [4,19]. The formation of the chromitite bodies is related to local slab tear, allowing rapid uprise of asthenospheric melts into the supra-subduction mantle wedges. In this model, chromite grains are interpreted to be transported against gravity attached to H<sub>2</sub>O-rich pools segregated from the basaltic melt [19]. Nevertheless, exsolution of volatiles to transport chromite grains necessary to form the chromitite bodies would only occur at very low pressures in the shallow mantle [96], hence, making unlikely the transport of chromite (a dense mineral) for tens of hundreds of kilometers from the slab window to the shallow mantle. For Mercedita chromitite bodies, and similar to previous models, slab contamination fails to explain the relation of reduced mineral phases with serpentinization processes.



(iv) Lightning Strikes Exposed Chromitite Bodies.

On the basis of experimental work using 30 kA electric discharges corresponding to natural cloud-to-ground lightning strikes [21,22], some have suggested that a suite of minerals of the SuR assemblage (such as moissanite and other carbides, silicides, alloys, and silicate and oxide spherules) can form in ophiolitic chromitite in response to lightning strikes. According to these authors, chromitite bodies within ophiolites are highly conductive and, hence, the thermal effect of a lightning strike could penetrate deeply if they are exposed at the Earth's surface. The derived >6000 K (5700 °C) thermal effect would produce plasma from which the aforementioned SuR phases and diamond precursors crystallize. However, if these high temperatures were reached during lightning (either experimental or natural), one could expect that chromite would melt and thus producing microstructural and chemical modifications, which have not been identified in natural chromites. It is worth to note that these experiments were performed using a silicate material, not chromite, therefore limiting its applicability to natural chromite as long as lightning strikes must have affected the entire rock and not only the silicate matrix. In addition, these authors state that "other high-pressure phases like coesite and stishovite may also form even though they are not found here", therefore leaving unexplained how plasma ejecta could form coesite intimately intergrown with diopside, as reported as oriented inclusions in the Tibetan chromitites, e.g., [65]. Moreover, the Mercedita chromitites were not exposed to lightning strikes and to the formation of fulgurite at the high altitude, in excess of 4000 m, suggested by [21,22] for the Tibetan case. The limited applicability of this model to explain the SuR minerals in the Mercedita chromitites is, again, the fact that SuR minerals occur associated with serpentine minerals, in both the silicate matrix and in fractures at Mercedita. These minerals formed at less than 700 °C, while fractures were annealed by recrystallization of chromite at subsolidus conditions during their passage through the shallow mantle and their final emplacement into the continental margin. These observations therefore rule out an origin of SuR minerals related to vaporization at the high temperatures proposed by Ballhaus and co-workers. Moreover, this model cannot explain the presence of minerals derived from the continental crust.

(v) The Cold Plumes Model.

Cold plumes comprise partially molten hydrated peridotite, dry solid mantle, and subducted oceanic crust [30,97] and references therein. Cold plumes rise in the mantle wedge as a result of Raleigh-Taylor instabilities caused by hydration and melting in the subduction channel [97]. The rise from a depth greater than 100 km brings asthenospheric and lithospheric mantle and subducted crustal material to shallow mantle levels, creating mineralogical and lithological heterogeneities in the mantle wedge. These heterogeneities may include bodies of podiform chromitite. Cold plumes are an excellent mechanism to transfer subducted crystals of zircon of crustal origin toward the mantle wedge [98], whereas others [16] explain the presence of crustal zircon in the Mayarí-Baracoa ophiolitic belt by this mechanism. Although this mechanism explains the presence of continental-crust-derived mineral phases, it fails to explain UHP and SuR minerals. For the case of the Mercedita chromitite, the presence of the crustal minerals can be explained by this model but the association of SuR phases and serpentinization-related minerals and the presence of the clinopyroxene lamellae along crystallographic planes of chromite cannot be explained.

## 6. Concluding Remarks

"Exotic" mineral phases in the Mercedita chromitite could be interpreted as providing evidence of high-pressure and ultra-reduced conditions (graphite-like amorphous carbon, clinopyroxene exsolution lamellae, moissanite, native elements, and alloys). However, the juxtaposition of chromitite bodies with unmetamorphosed gabbro sills rules out the possibility of deep recycling of the ophiolitic sequence. Evidence of a mantle plume, asthenospheric rise or lightning strikes can also hardly be invoked to the case of the ophiolites of eastern Cuba.

A simpler explanation for the formation of the “exotic” phases in the Mercedita chromitites can be offered. Clinopyroxene and rutile exsolution-induced lamellae formed during cooling of chromite after interaction with adjacent gabbros. The SuR phases (moissanite, native Cu, Fe–Mn alloy) formed during the serpentinization processes, where super-reduced microenvironments are created at low temperature and low pressure. Finally, crustal phases (corundum, quartz, zircon) represent sediment-derived xenocrystic grains delivered into the mantle wedge by cold plumes.

**Author Contributions:** J.A.P. conceived the ideas for this study; J.A.P., J.C.M. and F.G. participated in the field work and sample collection; A.A. designed the strategy for the XRD analyses; N.P.-S., J.A.P., A.G.-C. and J.M.G.-J. analyzed and discussed the resulting data; N.P.-S., J.A.P., A.G.-C. and J.M.G.-J. wrote the paper.

**Funding:** This research was financially supported by the Spanish Project CGL2015-65824 granted by the Spanish “Ministerio de Economía y Competitividad” to J.A.P., the Ramón y Cajal Fellowship RYC-2015-17596 to J.M.G.-J. and a FPU Ph.D grant to N.P.-S. by the Ministerio de Educación of the Spanish Government.

**Acknowledgments:** We want to thank three anonymous reviewers and the academic editor for their criticism that greatly improved our manuscript.

**Conflicts of Interest:** The authors declare no conflict of interest.

## References

- Robinson, P.T.; Bai, W.J.; Malpas, J.; Yang, J.S.; Zhou, M.F.; Fang, Q.S.; Hu, X.F.; Cameron, S.; Staudigel, H. Ultra-high pressure minerals in the Luobusa ophiolite, Tibet, and their tectonic implications. *Geol. Soc. Lond. Spec. Publ.* **2004**, *226*, 247–271. [[CrossRef](#)]
- Yang, J.S.; Dobrzhinetskaya, L.; Bai, W.J.; Fang, Q.S.; Robinson, P.T.; Zhang, J.; Green, H.W. Diamond- and coesite-bearing chromitites from the Luobusa ophiolite, Tibet. *Geology* **2007**, *35*, 875–878. [[CrossRef](#)]
- Dobrzhinetskaya, L.F.; Wirth, R.; Yang, J.; Hutcheon, I.D.; Weber, P.K.; Green, H.W. High-pressure highly reduced nitrides and oxides from chromitite of a Tibetan ophiolite. *Proc. Natl. Acad. Sci. USA* **2009**, *106*, 19233–19238. [[CrossRef](#)] [[PubMed](#)]
- Robinson, P.T.; Trumbull, R.B.; Schmitt, A.; Yang, J.S.; Li, J.W.; Zhou, M.F.; Erzinger, J.; Dare, S.; Xiong, F. The origin and significance of crustal minerals in ophiolitic chromitites and peridotites. *Gondwana Res.* **2015**, *27*, 486–506. [[CrossRef](#)]
- Xu, X.; Yang, J.; Robinson, P.T.; Xiong, F.; Ba, D.; Guo, G. Origin of ultrahigh pressure and highly reduced minerals in podiform chromitites and associated mantle peridotites of the Luobusa ophiolite, Tibet. *Gondwana Res.* **2015**, *27*, 686–700. [[CrossRef](#)]
- Yang, J.S.; Meng, F.; Xu, S.; Robinson, P.T.; Dilek, Y.; Makeyev, A.B.; Wirth, R.; Wiedenbeck, M.; Cliff, J. Diamonds, native elements and metal alloys from chromitite of the Ray-Iz ophiolite of the Polar Urals. *Gondwana Res.* **2015**, *27*, 459–485. [[CrossRef](#)]
- Zhang, R.Y.; Yang, J.S.; Ernst, W.G.; Jahn, B.M.; Iizuka, Y.; Guo, G.L. Discovery of in situ super-reducing, ultrahigh-pressure phases in the Luobusa ophiolitic chromitites, Tibet: New insights into the deep upper mantle and mantle transition zone. *Am. Mineral.* **2016**, *101*, 1285–1294. [[CrossRef](#)]
- Xiong, F.; Yang, J.; Robinson, P.T.; Xu, X.; Ba, D.; Li, Y.; Zhang, Z.; Rong, H. Diamonds and other exotic minerals recovered from peridotites of the Dangqiong Ophiolite, western Yarlung–Zangbo suture zone, Tibet. *Acta Geol. Sin.* **2016**, *90*, 425–439.
- Xiong, F.; Yang, J.; Dilek, Y.; Xu, X.; Zhang, Z. Origin and significance of diamonds and other exotic minerals in the Dingqing ophiolite peridotites, eastern Bangong–Nujiang suture zone, Tibet. *Lithosphere* **2017**, *10*, 142–155. [[CrossRef](#)]
- Lian, D.; Yang, J.; Dilek, Y.; Wu, W.; Zhang, Z.; Xiong, F.; Liu, F.; Zhou, W. Diamond, moissanite and other unusual minerals in podiform chromitites from Pozanti-Karsanti ophiolite, southern Turkey: Implications for deep mantle origin and ultra-reducing conditions in podiform chromitite. *Am. Mineral.* **2017**, *112*, 1101–1114.
- Akbulut, M. Investigation of silicate micro-inclusions from Orhaneli and Harmancik chromitites (NW Turkey): New ultrahigh-pressure evidence from Western Tethyan ophiolitic chromitites. *Ophioliti* **2018**, *43*, 1–22.

12. González-Jiménez, J.M.; Camprubí, A.; Colás, V.; Griffin, W.L.; Proenza, J.A.; O'Reilly, S.Y.; Centeno-García, E.; García-Casco, A.; Belousova, E.; Talavera, C.; et al. The recycling of chromitites in ophiolites from southwestern North America. *Lithos* **2017**, *294*, 53–72. [[CrossRef](#)]
13. Arai, S. Conversion of low-pressure chromitites to ultrahigh-pressure chromitites by deep recycling: A good inference. *Earth Planet. Sci. Lett.* **2013**, *397*, 81–87. [[CrossRef](#)]
14. McGowan, N.M.; Griffin, W.L.; González-Jiménez, J.M.; Belousova, E.A.; Afonso, J.; Shi, R.; McCammon, C.A.; Pearson, N.J.; O'Reilly, S.Y. Tibetan chromitites: Excavating the slab graveyard. *Geology* **2015**, *43*, 179–182. [[CrossRef](#)]
15. Griffin, W.L.; Afonso, J.C.; Belousova, E.A.; Gain, S.E.; Gong, X.H.; González-Jiménez, J.M.; Howell, D.; Huang, J.X.; McGowan, N.; Pearson, N.J.; et al. Mantle recycling: Transition zone metamorphism of Tibetan ophiolitic peridotites and its tectonic implications. *J. Petrol.* **2016**, *57*, 655–684. [[CrossRef](#)]
16. Proenza, J.A.; González-Jiménez, J.M.; García-Casco, A.; Belousova, E.; Griffin, W.L.; Talavera, C.; Rojas-Agramonte, Y.; Aiglsperger, T.; Navarro-Ciurana, D.; Pujol-Solà, N.; et al. Cold plumes trigger contamination of oceanic mantle wedges with continental crust-derived sediments: Evidence from chromitite zircon grains of eastern Cuban Ophiolites. *Geosci. Front.* **2018**, in press. [[CrossRef](#)]
17. Yang, J.S.; Robinson, P.T.; Dilek, Y. Diamonds in ophiolites. *Elements* **2014**, *10*, 127–130. [[CrossRef](#)]
18. Xiong, F.; Yang, J.; Robinson, P.T.; Xu, X.; Liu, Z.; Li, Y.; Li, J.; Chen, S. Origin of podiform chromitite, a new model based on the Luobusa ophiolite, Tibet. *Gondwana Res.* **2015**, *27*, 525–542. [[CrossRef](#)]
19. Zhou, M.F.; Robinson, P.T.; Su, B.X.; Gao, J.F.; Li, J.W.; Yang, J.S.; Malpas, J. Compositions of chromite, associated minerals, and parental magmas of podiform chromite deposits: The role of slab contamination of asthenospheric melts in suprasubduction zone environments. *Gondwana Res.* **2014**, *26*, 262–283. [[CrossRef](#)]
20. Johan, Z.; Martin, R.F.; Ettler, V. Fluids are bound to be involved in the formation of ophiolitic chromite deposits. *Eur. J. Mineral.* **2017**, *27*, 543–555. [[CrossRef](#)]
21. Ballhaus, C.; Wirth, R.; Fonseca, R.O.C.; Blanchard, H.; Pröll, W.; Bragagni, A.; Nagel, T.; Schreiber, A.; Dittrich, S.; Thome, V.; et al. Ultra-high pressure and ultra-reduced minerals in ophiolites may form by lightning strikes. *Geochem. Persp. Lett.* **2017**, *5*, 42–46. [[CrossRef](#)]
22. Ballhaus, C.; Fonseca, R.O.C.; Bragagni, A. Reply to Comment on “Ultra-high pressure and ultra-reduced minerals in ophiolites may form by lightning strikes” by Griffin et al. 2018: No evidence for transition zone metamorphism in the Luobusa ophiolite. *Geochem. Persp. Lett.* **2018**, *7*, 3–4. [[CrossRef](#)]
23. Iturralde-Vinent, M. (Ed.) Introduction to Cuban geology and geophysics. In *Ophiolitas y Arcos Volcánicos de Cuba*; International Geological Correlation Programme: Miami, FL, USA, 1996; Volume 364, pp. 3–35.
24. Proenza, J.A.; Gervilla, F.; Melgarejo, J.C.; Bodinier, J.L. Al- and Cr-rich chromitites from the Mayarí-Baracoa ophiolitic belt (eastern Cuba); consequence of interaction between volatile-rich melts and peridotites in suprasubduction mantle. *Econ. Geol.* **1999**, *94*, 547–566. [[CrossRef](#)]
25. Iturralde-Vinent, M.A.; Díaz-Otero, C.; Rodríguez-Vega, A.; Díaz-Martínez, R. Tectonic implications of paleontologic dating of Cretaceous–Danian sections of Eastern Cuba. *Geol. Acta* **2006**, *4*, 89–102.
26. García-Casco, A.; Torres-Roldán, R.L.; Iturralde-Vinent, M.A.; Millán, G.; Núñez Cambra, K.; Lázaro, C.; Rodríguez Vega, A. High pressure metamorphism of ophiolites in Cuba. *Geol. Acta* **2006**, *4*, 63–88.
27. García-Casco, A.; Iturralde-Vinent, M.A.; Pindell, J. Latest Cretaceous collision/accretion between the Caribbean Plate and Caribbeana: Origin of metamorphic terranes in the Greater Antilles. *Int. Geol. Rev.* **2008**, *50*, 781–809. [[CrossRef](#)]
28. García-Casco, A.; Lázaro, C.; Torres-Roldán, R.L.; Núñez Cambra, K.; Rojas Agramonte, Y.; Kröner, A.; Neubauer, F.; Millán, G.; Blanco-Quintero, I. Partial melting and counterclockwise P-T path of subducted oceanic crust (Sierra del Convento mélange, Cuba). *J. Petrol.* **2008**, *49*, 129–161. [[CrossRef](#)]
29. Lázaro, C.; García-Casco, A.; Rojas-Agramonte, Y.; Kröner, A.; Neubauer, F.; Iturralde-Vinent, M. Fifty-five-million-year history of oceanic subduction and exhumation at the northern edge of the Caribbean plate (Sierra del Convento mélange, Cuba). *J. Metamorph. Geol.* **2009**, *27*, 19–40. [[CrossRef](#)]
30. Blanco-Quintero, I.F.; Gerya, T.V.; García-Casco, A.; Castro, A. Subduction of young oceanic plates: A numerical study with application to aborted thermal-chemical plumes. *Geochem. Geophys.* **2011**, *12*, 10.
31. Blanco-Quintero, I.F.; Proenza, J.A.; García-Casco, A.; Tauler, E.; Galí, S. Serpentinites and serpentinites within a fossil subduction channel: La Corea mélange, eastern Cuba. *Geol. Acta* **2011**, *9*, 389–405.

32. Blanco-Quintero, I.F.; Rojas-Agramonte, Y.; García-Casco, A.; Kröner, A.; Mertz, D.F.; Lázaro, C.; Blanco-Moreno, J.; Renne, P.R. Timing of subduction and exhumation in a subduction channel: Evidence from slab melts from La Corea mélangé (eastern Cuba). *Lithos* **2011**, *127*, 86–100. [[CrossRef](#)]
33. Lázaro, C.; García-Casco, A.; Blanco-Quintero, I.F.; Rojas-Agramonte, Y.; Corsini, M.; Proenza, J.A. Did the Turonian–Coniacian plume pulse trigger subduction initiation in the Northern Caribbean? Constraints from <sup>40</sup>Ar/<sup>39</sup>Ar dating of the Moa-Baracoa metamorphic sole (eastern Cuba). *Int. Geol. Rev.* **2015**, *57*, 919–942. [[CrossRef](#)]
34. Cárdenas-Párraga, J.; García-Casco, A.; Proenza, J.A.; Harlow, G.E.; Blanco-Quintero, I.F.; Lázaro, C.; Villanova-de-Benavent, C.; Núñez Cambra, K. Trace-element geochemistry of transform-fault serpentinite in high-pressure subduction mélanges (eastern Cuba): Implications for subduction initiation. *Int. Geol. Rev.* **2017**, *59*, 2041–2064. [[CrossRef](#)]
35. Iturralde-Vinent, M.A.; Diaz Otero, C.; García-Casco, A.; Van Hinsbergen, D.J.J. Paleogene foredeep basin deposits of North-Central Cuba: A record of arc-continent collision between the Caribbean and North American plate. *Int. Geol. Rev.* **2008**, *50*, 863–884. [[CrossRef](#)]
36. Van Hinsbergen, D.J.J.; Iturralde-Vinent, M.A.; Van Geffen, P.W.; García-Casco, A.; Van Benthem, S. Structure of the accretionary prism, and the evolution of the Paleogene northern Caribbean subduction zone in the region of Camagüey, Cuba. *J. Struct. Geol.* **2009**, *31*, 1130–1144. [[CrossRef](#)]
37. Lewis, J.F.; Draper, G.; Proenza, J.A.; Espaillet, J.; Jiménez, J. Ophiolite-related ultramafic rocks (serpentinites) in the Caribbean region: A review of their occurrence, composition, origin, emplacement and nickel laterite soils. *Geol. Acta* **2006**, *4*, 237–263.
38. Marchesi, C.; Garrido, C.J.; Godard, M.; Proenza, J.A.; Gervilla, F.; Blanco-Moreno, J. Petrogenesis of highly depleted peridotites and gabbroic rocks from the Mayarí-Baracoa Ophiolitic Belt (eastern Cuba). *Contrib. Mineral. Petrol.* **2006**, *151*, 717–736. [[CrossRef](#)]
39. Iturralde-Vinent, M.A.; García-Casco, A.; Rojas-Agramonte, Y.; Proenza, J.A.; Murphy, J.B.; Stern, R.G. The geology of Cuba: A brief overview and synthesis. *GSA Today* **2016**, *26*, 4–10. [[CrossRef](#)]
40. Proenza, J.A.; Díaz-Martínez, R.; Iriondo, A.; Marchesi, C.; Melgarejo, J.C.; Gervilla, F.; Garrido, C.J.; Rodríguez-Vega, A.; Lozano-Santacruz, R.; Blanco-Moreno, J.A. Primitive island-arc Cretaceous volcanic rocks in eastern Cuba: The Téneme Formation. *Geol. Acta* **2006**, *4*, 103–121.
41. Gervilla, F.; Proenza, J.A.; Frei, R.; González-Jiménez, J.M.; Garrido, C.J.; Melgarejo, J.C.; Meibom, A.; Díaz-Martínez, R.; Lavaut, W. Distribution of platinum-group elements and Os isotopes in chromite ores from Mayarí-Baracoa Ophiolitic Belt (eastern Cuba). *Contrib. Mineral. Petrol.* **2005**, *150*, 589–607. [[CrossRef](#)]
42. Marchesi, C.; Garrido, C.J.; Bosch, D.; Proenza, J.A.; Gervilla, F.; Monié, P.; Rodríguez-Vega, A. Geochemistry of Cretaceous magmatism in eastern Cuba: Recycling of North American continental sediments and implications for subduction polarity in the Greater Antilles Paleo-arc. *J. Petrol.* **2007**, *48*, 1813–1840. [[CrossRef](#)]
43. González-Jiménez, J.M.; Proenza, J.A.; Gervilla, F.; Melgarejo, J.C.; Blanco-Moreno, J.A.; Ruiz-Sánchez, R.; Griffin, W.L. High-Cr and high-Al chromitites from the Sagua de Tánamo district, Mayarí-Cristal Ophiolitic Massif (eastern Cuba): Constraints on their origin from mineralogy and geochemistry of chromian spinel and platinum group elements. *Lithos* **2011**, *125*, 101–121. [[CrossRef](#)]
44. Proenza, J.A.; Gervilla, F.; Melgarejo, J.C.; Revé, D.; Rodríguez, G. Las cromititas ofiolíticas del yacimiento Mercedita (Cuba). Un ejemplo de cromitas ricas en Al en la zona de transición manto-corteza. *Acta Geol. Hisp.* **1998**, *33*, 179–212.
45. Guild, P.W. Petrology and structure of the Moa Chromite District, Oriente province, Cuba. *Trans. Am. Geophys. Union* **1947**, *28*, 218–246. [[CrossRef](#)]
46. Flint, D.E.; de Albear, J.F.; Guild, P.W. *Geology and Chromite Deposits of the Camagüey District, Camagüey Province, Cuba*; U.S. Geological Survey Bull: Washington, DC, USA, 1948; Volume 954-B, pp. 39–63.
47. Leblanc, M.; Violette, J.F. Distribution of aluminium-rich and chromium-rich chromite pods in ophiolite peridotites. *Econ. Geol.* **1983**, *78*, 293–301. [[CrossRef](#)]
48. Aiglsperger, T.; Proenza, J.A.; Zaccarini, F.; Lewis, J.F.; Garuti, G.; Labrador, M.; Longo, F. Platinum group minerals (PGM) in the Falcondo Ni laterite deposit, Loma Caribe peridotite (Dominican Republic). *Miner. Depos.* **2015**, *50*, 105–123. [[CrossRef](#)]
49. Pouchou, J.L.; Pichoir, F. Quantitative analysis of homogeneous or stratified microvolumes applying the model PAP. In *Electron Probe Quantitation*; Heinrich, K.J., Newbury, D.E., Eds.; Plenum Press: New York, NY, USA, 1991; pp. 31–75, ISBN 978-1-4899-2619-7.

50. Proenza, J.A.; Alfonso, P.; Melgarejo, J.C.; Gervilla, F.; Tritlla, J.; Fallick, A.E. D., O and C isotopes in podiform chromitites as fluid tracers for hydrothermal alteration processes of the Mayarí-Baracoa Ophiolitic Belt, eastern Cuba. *J. Geochem. Explor.* **2003**, *78–79*, 1–6. [[CrossRef](#)]
51. Irvine, T.N. Chromian spinel as a petrogenetic indicator: Part 2. Petrologic applications. *Can. J. Earth Sci.* **1967**, *4*, 71–103. [[CrossRef](#)]
52. Leblanc, M.; Nicolas, A. Ophiolitic chromitites. *Int. Geol. Rev.* **1992**, *34*, 653–686. [[CrossRef](#)]
53. Bonavia, F.F.; Diella, V.; Ferrario, A. Precambrian podiform chromitites from Kenticha Hill, southern Ethiopia. *Econ. Geol.* **1993**, *88*, 198–202. [[CrossRef](#)]
54. Arai, S.; Uesugi, J.; Ahmed, A.H. Upper crustal podiform chromitite from the northern Oman ophiolite as the stratigraphically shallowest chromitite in ophiolite and its implication for Cr concentration. *Contrib. Mineral. Petrol.* **2004**, *147*, 145–154. [[CrossRef](#)]
55. Arai, S. Chemistry of chromian spinel in volcanic rocks as a potential guide to magma chemistry. *Mineral. Mag.* **1992**, *56*, 173–184. [[CrossRef](#)]
56. Prencipe, M.; Mantovani, L.; Tribaudino, M.; Bersani, D.; Lottici, P.P. The Raman spectrum of diopside: A comparison between ab initio calculated and experimentally measured frequencies. *Eur. J. Mineral.* **2012**, *24*, 457–464. [[CrossRef](#)]
57. Shiryaev, A.A.; Griffin, W.L.; Stoyanov, E. Moissanite (SiC) from kimberlites: Polytypes, trace elements, inclusions and speculations on origin. *Lithos* **2011**, *122*, 152–164. [[CrossRef](#)]
58. Trumbull, R.B.; Yang, J.S.; Robinson, P.T.; Di Pierro, S.; Vennemann, T.; Wiedenbeck, M. The carbon isotope composition of natural SiC (moissanite) from the Earth's mantle: New discoveries from ophiolites. *Lithos* **2009**, *113*, 612–620. [[CrossRef](#)]
59. Xu, S.T.; Wu, W.P.; Xiao, W.S.; Yang, J.S.; Chen, J.; Ji, S.Y.; Liu, Y.C. Moissanite in serpentinite from the Dabie Mountains in China. *Mineral. Mag.* **2008**, *72*, 899–908. [[CrossRef](#)]
60. Tian, Y.; Yang, J.; Robinson, P.T.; Xiong, F.; Yuan, L.L.; Zhang, Z.; Liu, Z.; Liu, F.; Niu, X. Diamond discovered in high-Al chromitites of the Sartohay Ophiolite, Xinjiang Province, China. *Acta Geol. Sin.* **2015**, *89*, 332–340.
61. Yamamoto, S.; Komiya, T.; Hirose, K.; Maruyama, S. Coesite and clinopyroxene exsolution lamellae in chromites: In-situ ultrahigh-pressure evidence from podiform chromitites in the Luobusa ophiolite, southern Tibet. *Lithos* **2009**, *109*, 314–322. [[CrossRef](#)]
62. Miura, M.; Arai, S.; Ahmed, A.H.; Mizukami, T.; Okuno, M.; Yamamoto, S. Podiform chromitite classification revisited: A comparison of discordant and concordant chromitite pods from Wadi Hilti, northern Oman ophiolite. *J. Asian Earth Sci.* **2012**, *59*, 52–61. [[CrossRef](#)]
63. Arai, S.; Miura, M. Formation and modification of chromitites in the mantle. *Lithos* **2016**, *264*, 277–295. [[CrossRef](#)]
64. Ono, S.; Kikegawa, T.; Higo, Y.; Tange, Y. Precise determination of the phase boundary between coesite and stishovite in SiO<sub>2</sub>. *Phys. Earth Planet. Int.* **2017**, *264*, 1–6. [[CrossRef](#)]
65. Satsukawa, T.; Griffin, W.L.; Piazzolo, S.; O'Reilly, S.Y. Messengers from the deep: Fossil wadsleyite–chromite microstructures from the Mantle Transition Zone. *Sci. Rep.* **2015**, *5*, 16484. [[CrossRef](#)] [[PubMed](#)]
66. Wu, Y.; Xu, M.; Jin, Z.; Fei, Y.; Robinson, P.T. Experimental constraints on the formation of the Tibetan podiform chromitites. *Lithos* **2016**, *245*, 109–117. [[CrossRef](#)]
67. Zhang, Y.F.; Jin, Z.M.; Griffin, W.L.; Wang, C.; Wu, Y. High-pressure experiments provide insights into the Mantle Transition Zone history of chromitite in Tibetan ophiolites. *Earth Planet. Sci. Lett.* **2017**, *463*, 151–158. [[CrossRef](#)]
68. Chen, M.; Shu, J.; Xie, X.; Mao, H.K. Natural CaTi<sub>2</sub>O<sub>4</sub>-structured FeCr<sub>2</sub>O<sub>4</sub> polymorph in the Suizhou meteorite and its significance in mantle mineralogy. *Geochim. Cosmochim. Acta* **2003**, *67*, 3937–3942. [[CrossRef](#)]
69. Cameron, E.N. Titanium-bearing oxide minerals of the Critical Zone of the Eastern Bushveld Complex. *Am. Miner.* **1979**, *64*, 140–150.
70. Arai, S.; Yurimoto, H. Podiform chromitites of the Tari–Misaka ultramafic complex, Southwest Japan, as mantle-melt interaction products. *Econ. Geol.* **1994**, *89*, 1279–1288. [[CrossRef](#)]
71. Augé, T. Chromite deposits in the northern Oman ophiolite: Mineralogical constraints. *Miner. Depos.* **1987**, *22*, 1–10. [[CrossRef](#)]
72. Xiong, Q.; Griffin, W.L.; Huang, J.X.; Gain, S.E.; Toledo, V.; Pearson, N.J.; O'Reilly, S.Y. Super-reduced mineral assemblages in “ophiolitic” chromitites and peridotites: The view from Mount Carmel. *Eur. J. Mineral.* **2017**, *29*, 557–570. [[CrossRef](#)]

73. Yang, J.S.; Xu, X.Z.; Li, Y.; Li, J.Y.; Ba, D.Z.; Rong, H.; Zhang, Z.M. Diamonds recovered from peridotite of the Purang ophiolite in the Yarlung-Zangbo suture of Tibet: A proposal for a new type of diamond occurrence. *Acta Petrol. Sin.* **2011**, *27*, 3171–3178.
74. Xiong, Q.; Henry, H.; Griffin, W.L.; Zheng, J.P.; Satsukawa, T.; Pearson, N.J.; O'Reilly, S.Y. High- and low-Cr chromitite and dunite in a Tibetan ophiolite: Evolution from mature subduction system to incipient forearc in the Neo-Tethyan Ocean. *Contrib. Mineral. Petrol.* **2017**, *172*, 45. [[CrossRef](#)]
75. Xiong, F.; Yang, J.; Robinson, P.T.; Dilek, Y.; Milushi, I.; Xu, X.; Zhou, W.; Zhang, Z.; Rong, H. Diamonds Discovered from High-Cr Podiform Chromitites of Bulqiza, Eastern Mirdita Ophiolite, Albania. *Acta Geol. Sin. Eng. Ed.* **2017**, *91*, 455–468. [[CrossRef](#)]
76. Chen, Y.; Yang, J.; Xu, Z.; Tian, Y.; Lai, S. Diamonds and other unusual minerals from peridotites of the Myitkyina ophiolite, Myanmar. *J. Asian Earth Sci.* **2018**, *164*, 179–193. [[CrossRef](#)]
77. Bai, W.J.; Robinson, P.T.; Fang, Q.; Hu, X.F.; Zhou, M.F. The PGE and base-metal alloys in the podiform chromitites of the Luobusa ophiolite, southern Tibet. *Can. Mineral.* **2000**, *38*, 585–598. [[CrossRef](#)]
78. Alexander, C.M.O. Presolar SiC in chondrites: How variable and how many sources? *Geochim. Cosmochim. Acta* **1993**, *57*, 2869–2888. [[CrossRef](#)]
79. Moore, R.O.; Otter, M.L.; Rickard, R.S.; Harris, J.W.; Gurney, J.J. The occurrence of moissanite and ferro-periclase as inclusions in diamond. In Proceedings of the 4th International Kimberlite Conference, Perth, Australia, 11–15 August 1986; pp. 409–411.
80. Moore, R.O.; Gurney, J.J. Mineral inclusions in diamond from the Monastery kimberlite, South Africa. *Kimberl. Relat. Rocks* **1989**, *2*, 1029–1041.
81. Leung, I.S. Silicon carbide cluster entrapped in a diamond from Fuxian, China. *Am. Mineral.* **1990**, *75*, 1110–1119.
82. Kaminsky, F. Mineralogy of the lower mantle: A review of 'super-deep' mineral inclusions in diamond. *Earth Sci. Rev.* **2012**, *110*, 127–147. [[CrossRef](#)]
83. Di Pierro, S.; Gnos, E.; Grobety, B.H.; Armbruster, T.; Bernasconi, S.M.; Ulmer, P. Rock-forming moissanite (natural alpha-silicon carbide). *Am. Mineral.* **2003**, *88*, 1817–1821. [[CrossRef](#)]
84. Dobrzhinetskaya, L.; Mukhin, P.; Wang, Q.; Wirth, R.; O'Bannon, E.; Zhao, W.; Eppelbaum, L.; Sokhonchuk, T. Moissanite (SiC) with metal-silicide and silicon inclusions from tuff of Israel: Raman spectroscopy and electron microscope studies. *Lithos* **2017**, *310–311*, 355–368. [[CrossRef](#)]
85. Machev, P.; O'Bannon, E.; Bozhilov, K.; Wang, Q.; Dobrzhinetskaya, L. Not all moissanites are created equal: New constraints on moissanite from metamorphic rocks of Bulgaria. *Earth Planet. Sci. Lett.* **2018**, *498*, 387–396. [[CrossRef](#)]
86. Gnoevaja, N.; Grozdanov, L. Moissanite from Triassic rocks, NW Bulgaria. *Proc. Bulg. Geol. Soc.* **1965**, *26*, 89–95.
87. Shiryaev, A.A.; Wiedenbeck, M.; Reutsky, V.; Polyakov, V.B.; Mel'nik, N.N.; Lebedev, A.A.; Yakimova, R. Isotopic heterogeneity in synthetic and natural silicon carbide. *J. Phys. Chem. Solids* **2008**, *69*, 2492–2498. [[CrossRef](#)]
88. Schmidt, M.W.; Gao, C.; Golubkova, A.; Rohrbach, A.; Connolly, J.A. Natural moissanite (SiC)—A low temperature mineral formed from highly fractionated ultra-reducing COH-fluids. *Prog. Earth Planet. Sci.* **2014**, *1*, 27. [[CrossRef](#)]
89. Golubkova, A.; Schmidt, M.W.; Connolly, J.A. Ultra-reducing conditions in average mantle peridotites and in podiform chromitites: A thermodynamic model for moissanite (SiC) formation. *Contrib. Mineral. Petrol.* **2016**, *171*, 41. [[CrossRef](#)]
90. Sachan, H.K.; Mukherjee, B.K.; Bodnar, R.J. Preservation of methane generated during serpentinization of upper mantle rocks: Evidence from fluid inclusions in the Nidar ophiolite, Indus Suture Zone, Ladakh (India). *Earth Planet. Sci. Lett.* **2007**, *257*, 47–59. [[CrossRef](#)]
91. Kelley, D.S.; Früh-Green, G.L. Abiogenic methane in deep-seated mid-ocean ridge environments: Insights from stable isotope analyses. *J. Geophys. Res.* **1999**, *104*, 10439–10460. [[CrossRef](#)]
92. Melcher, F.; Grum, W.; Simon, G.; Thalhammer, T.V.; Stumpfl, E. Petrogenesis of the ophiolitic giant chromite deposit of Kempirsai, Kazakhstan: A study of solid and fluid inclusions in chromite. *J. Petrol.* **1997**, *10*, 1419–1458. [[CrossRef](#)]
93. Proenza, J.A. Mineralizaciones de Cromita en la Faja Ofiolítica Mayarí-Baracoa (Cuba). Ejemplo del Yacimiento Mercedita. Ph.D. Thesis, Universitat de Barcelona, Barcelona, Spain, February 1998; p. 227.

94. Rojas-Agramonte, Y.; Williams, I.S.; Arculus, R.; Kröner, A.; García-Casco, A.; Lázaro, C.; Buhre, S.; Wong, J.; Geng, H.; Morales Echevarría, C.; et al. Ancient xenocrystic zircon in young volcanic rocks of the southern Lesser Antilles island arc. *Lithos* **2017**, *290*, 228–252. [[CrossRef](#)]
95. Ruskov, T.; Spirov, I.; Georgieva, M.; Yamamoto, S.; Green, H.W.; McCammon, C.A.; Dobrzhinetskaya, L.F. Mossbauer spectroscopy studies of the valence state of iron in chromite from the Luobusa massif of Tibet: Implications for a highly reduced deep mantle. *J. Metamorph. Geol.* **2010**, *28*, 551–560. [[CrossRef](#)]
96. Matveev, S.; Ballhaus, C. Role of water in the origin of podiform chromitite deposits. *Earth Planet. Sci. Lett.* **2002**, *203*, 235–243. [[CrossRef](#)]
97. Gerya, T.V.; Yuen, D. Rayleigh–Taylor instabilities from hydration and melting propel “cold plumes” at subduction zones. *Earth Planet. Sci. Lett.* **2003**, *212*, 47–62. [[CrossRef](#)]
98. Rojas-Agramonte, Y.; Garcia-Casco, A.; Kemp, A.; Kröner, A.; Proenza, J.A.; Lázaro, C.; Liu, D. Recycling and transport of continental material through the mantle wedge above subduction zones: A. Caribbean example. *Earth Planet. Sci. Lett.* **2016**, *436*, 93–107. [[CrossRef](#)]



© 2018 by the authors. Licensee MDPI, Basel, Switzerland. This article is an open access article distributed under the terms and conditions of the Creative Commons Attribution (CC BY) license (<http://creativecommons.org/licenses/by/4.0/>).